School of Natural Sciences and Mathematics
William B. Hanson Center for Space Sciences

Coordinated Satellite Observations of the Very Low Frequency Transmission through the Ionospheric D Layer at Low Latitudes, Using Broadband Radio Emissions from Lightning

UT Dallas Author(s):
Roderick A. Heelis

Citation:
Jacobson, Abram R., Robert H. Holzworth, Robert Pfaff, and Roderick Heelis. 2018. "Coordinated satellite observations of the very low frequency transmission through the ionospheric D layer at low latitudes, using broadband radio emissions from lightning." Journal of Geophysical Research: Space Physics 123(4): 2926-2952, doi:10.1002/2017JA024942

Journal of Geophysical Research: Space Physics

RESEARCH ARTICLE
10.1002/2017JA024942

Key Points:
- Lightning radio emissions are used to probe the ionospheric *D* layer's radio transmission at low latitudes
- The main tools in this study are the C/NOFS satellite and the World Wide Lightning Location Network
- We find sporadic enhanced transmission of VLF waves, well beyond the level predicted by laminar-ionosphere models

Correspondence to:
A. R. Jacobson,
abramj@uw.edu

Citation:
Jacobson, A. R., Holzworth, R. H., Pfaff, R., & Heelis, R. (2018). Coordinated satellite observations of the very low frequency transmission through the ionospheric *D* layer at low latitudes, using broadband radio emissions from lightning. *Journal of Geophysical Research: Space Physics*, *123*, 2926–2952. https://doi.org/10.1002/2017JA024942

Received 2 NOV 2017
Accepted 9 MAR 2018
Accepted article online 13 MAR 2018
Published online 6 APR 2018

Coordinated Satellite Observations of the Very Low Frequency Transmission Through the Ionospheric *D* Layer at Low Latitudes, Using Broadband Radio Emissions From Lightning

Abram R. Jacobson[1], Robert H. Holzworth[1], Robert Pfaff[2], and Roderick Heelis[3]

[1]Earth and Space Sciences Department, University of Washington, Seattle, WA, USA, [2]NASA Goddard Space Flight Center, Greenbelt, MD, USA, [3]Hanson Center for Space Sciences, University of Texas at Dallas, Richardson, TX, USA

Abstract Both ray theory and full-wave models of very low frequency transmission through the ionospheric *D* layer predict that the transmission is greatly suppressed near the geomagnetic equator. We use data from the low-inclination Communication/Navigation Outage Forecast System satellite to test this semiquantitatively, for broadband very low frequency emissions from lightning. Approximate ground-truthing of the incident wavefields in the Earth-ionosphere waveguide is provided by the World Wide Lightning Location Network. Observations of the wavefields at the satellite are provided by the Vector Electric Field Instrument aboard the satellite. The data set comprises whistler observations with the satellite at magnetic latitudes $<26°$. Thus, our conclusions, too, must be limited to the near-equatorial region and are not necessarily predictive of midlatitude whistler properties. We find that in most broadband recordings of radio waves at the satellite, very few of the lightning strokes result in a detectable radio pulse at the satellite. However, in a minority of the recordings, there is enhanced transmission of very low frequency lightning emissions through the *D* layer, at a level exceeding model predictions by at least an order of magnitude. We show that kilometric-scale *D*-layer irregularities may be implicated in the enhanced transmission. This observation of sporadic enhancements at low magnetic latitude, made with broadband lightning emissions, is consistent with an earlier review of *D*-layer transmission for transmission from powerful man-made radio beacons.

1. Introduction

Our core goal in this article is to infer the degree of low-latitude upward transmission of lightning-generated, broadband VLF (very low frequency, specifically 5–14 kHz) from the Earth-ionosphere waveguide (EIWG), through the lower ionosphere, to a satellite. The satellite altitude, in this case, is in the midionosphere and upper ionosphere (400–850 km), deep in the innermost magnetosphere, so that the upward transmission of zero-hop whistlers is mainly limited by the *D*-layer effects (Helliwell, 2006). That transmission can be modeled by full-wave solutions assuming a vertically layered ionosphere and linear dielectric effects (Jacobson et al., 2010, 2009, 2012; Lehtinen & Inan, 2009; Nagano et al., 1975; Piggott et al., 1965; Pitteway, 1965). Observational tests of these full-wave models' transmission predictions have been sparse, particularly at very low magnetic latitudes. A notable exception is the comparison between predicted and measured signal amplitudes for several powerful ground-based, narrow-band transmitters, received by radio sensors on various high-inclination satellites (Starks et al., 2008). The discrete transmitter frequencies ranged from 13 to 25 kHz in that study, higher than the bulk of the frequency spectrum in our present broadband study (5–14 kHz). Moreover, there was a possibility of nonlinear electrical interactions with the *D*-layer electrons due to the exceptionally high transmitted power at narrow bandwidth (Bell et al., 2008; Foust et al., 2010). Such a nonlinear interaction is outside the scope of the linear-dielectric models.

A potentially important motivation for understanding VLF penetration through the lower ionosphere is better characterization of the interaction of VLF wavefields with particles in the magnetosphere. It has been previously pointed out that lightning frequently instigates prolonged broadband noise in the lower VLF spectrum (Sonwalkar & Inan, 1989). We see the same phenomenon in our data too, although it is not the subject of this article. If the instigated broadband noise, which lasts much longer than the duration of the lightning pulse itself, can functionally act like the "plasmaspheric hiss" (Meredith et al., 2006) that it resembles, then the instigated noise might also contribute to energizing electrons near the equatorial regions of low-latitude flux tubes.

The remainder of this paper is structured as follows: Section 2 reviews the systems from which this study derives its data. Section 3 describes the dominant control by the ionospheric *D* region over VLF upward transmission into the midionosphere and upper ionosphere. Section 4 documents a negative finding, which is key to understanding our results: Most of the Vector Electric Field Investigation (VEFI) observing records are devoid of detected lightning-generated whistlers that can be associated with strokes located by Worldwide Lightning Location Network (WWLLN). Section 5 describes the sampling of various geophysical independent variables by our VEFI data: geomagnetic inclination, propagation arc-distance in the EIWG, solar illumination along the propagation path, and magnetic azimuth of propagation.

2. The Joint Use of C/NOFS and WWLLN for this Study

2.1. The C/NOFS Satellite

The C/NOFS satellite (Communication/Navigation Outage Forecast System) (de La Beaujardiere, 2004) was a nadir-stabilized, nonspinning, low-Earth-orbit satellite in a slightly elliptical orbit at very low inclination (13°). It provided data from a suite of instruments from mission start in 2008 through end of mission in 2015. The primary instrument aboard C/NOFS for this study was VEFI, or Vector Electric Field Investigation (Pfaff et al., 2010). VEFI was designed, built, tested, and operated by the Goddard Space Flight Center of National Aeronautics and Space Administration.

VEFI recorded the electric field simultaneously along three orthogonal axes, in a variety of observing modes. The mode used in this study was the "burst recording mode" with about 32 kilosamples/s sampling rate. These burst recordings were typically 12 s duration, although occasionally longer. During each recording, the VLF electric field was continuously sampled. The recordings were not triggered by VLF activity, so they were not biased for times of strong VLF. Details on the lightning-VLF application of VEFI are available elsewhere (Jacobson et al., 2011, 2014, 2016; Pfaff et al., 2010). The recordings' times of occurrence were programmed in advance for mostly during local darkness and were not in any way whatsoever chosen to coincide with storms or lightning incidence. No physical signal was used to initiate recording. There should be no particular statistical association between these recordings' time/location and lightning time/location.

This article will present measurements of the time-integrated Poynting flux density, or the Poynting "fluence" density, in the ionosphere, during the passage of lightning-generated whistlers. In order for this to be worthwhile, we must have confidence in the accuracy and stability of the VEFI measurements of the wave electric fields. The VEFI system spectral transfer functions for all three channels, from DC to the Nyquist frequency (~16 kHz), were carefully calibrated prelaunch (Pfaff et al., 2010). However, for our purposes, we must address the question of whether the system gains of any of the three antenna/amplifier chains have drifted, shifted, or failed on-orbit. This could be due, were it to occur, to either a mechanical issue with an antenna boom or damage to any link in the amplifier chain. Is there a means of detecting such a failure on-orbit?

Fortunately, there is a convenient on-orbit means of checking that each channel's antenna and system gain are nominal. The three axes' respective antennas and amplifier chains are all mutually independent of each other. This has an important benefit for on-orbit validation of the electric field measurement: An on-orbit gain change in any one of these three antennas or amplifier chains is unlikely to be matched by an exactly identical gain change in the two other antennas. We developed a method to check on-orbit if any measurable differential system gain occurred between any two of the three channels (Jacobson et al., 2011, 2014). The method is based on the fact that VLF wave electric fields should be highly orthogonal to the background geomagnetic field. Using the International Geomagnetic Reference Field (IAGA, Division V, Working Group 8, 2003), we estimate the background vector magnetic field $\mathbf{B}_0$ at the satellite's instantaneous location. We then compute two time averages (over the entire record): the first of the square $<E^2_{\mathrm{par}}>$ of the wave electric field parallel to B_0 and the second of the square $<E^2_{\mathrm{perp}}>$ of the wave electric field normal to B_0. We require that ratio to be small, that is, $<E^2_{\mathrm{par}}>/<E^2_{\mathrm{perp}}>$ must not exceed 0.015. In fact, most of the records in the data set are much better than that upper limit; the median value of $<E^2_{\mathrm{par}}>/<E^2_{\mathrm{perp}}>$ is 0.003. Full details of this on-orbit test procedure have been presented elsewhere (Jacobson et al., 2011, 2014). We thus assure with a high degree of confidence that no antenna/amplifier chain has drifted or departed from tracking the other two. Given the total independence of the three antenna/amplifier chains, this gives a high degree of confidence in the stated system gains from prelaunch characterization.

We use VEFI data to infer the wave polarization and the whistler wavevector (Jacobson et al., 2014). This requires contemporaneous data on the composition of the major ion species (O+, H+, and He+) at the satellite. Those data are furnished to our analysis from the C/NOFS Ion Neutral Drift Investigation, or CINDI instrument (Heelis et al., 2009). CINDI ion-composition data are more than adequate for our purposes. In fact, we are able to independently check on CINDI's proper operation, by comparing with our own spectral data. The VEFI recordings frequently contain strong lower-hybrid wave activity at and slightly above the lower-hybrid resonance (LHR) frequency, with the lower margin crisply demarcated by the lower edge of the LHR activity on spectral displays. We compare that lower edge frequency with the calculated, multispecies LHR frequency using CINDI ion composition and modeled geomagnetic field. The agreement is near perfect, within 2%.

The determination of polarization allows us to infer the wavevector (Jacobson et al., 2014). The wavevector **k** direction is specified by two angles: first, the polar angle θ between **k** and $\mathbf{B}_0$ (the geomagnetic field) and second, the azimuthal angle of **k** rotated around $\mathbf{B}_0$, at constant θ. The refractive index depends on the polar but not on the azimuthal angle. The polar angle θ that we observe indicates oblique, rather than ducted, whistler transmission. Each identified whistler pulse has a narrowly defined pixel distribution of θ ($\pm 5°$ typically), but the central value of the distribution (for a given pulse) typically is in the range 40 to 85°. Values $\theta < 40°$ are seen only rarely. The bulk of the polar angles are closer to perpendicular than to parallel (with respect to $\mathbf{B}_0$). This indicates that the propagation is consistent with oblique, but not with ducted, propagation (Streltsov et al., 2006). This is also consistent with the fact that we analyze whistler data only during conditions of steady, undisturbed density as indicated by the Langmuir probe (Jacobson et al., 2014, 2016).

2.2. The WWLLN Ground-Truth

The WWLLN locates and times lightning strokes globally (Jacobson et al., 2006; Lay et al., 2004, 2007; Rodger et al., 2004, 2005, 2006). WWLLN is a collaborative network of over 60 sites hosted by institutions worldwide and is managed by Dr. R. Holzworth under the auspices of the University of Washington. More details can be obtained from the references above and from the facility's website (www.wwlln.net). WWLLN has a typical location accuracy on the order of 10 km, and timing accuracy on the order of 30 μs.

Since mid-2009, WWLLN has also provided estimates of the stroke radiated VLF energy (Hutchins et al., 2012, 2013). We limit our consideration of the VEFI recordings in this study to begin only after the startup of WWLLN VLF-energy estimates, so we do not use the data from the satellite's first year of mission. The energy estimate serves as a "ground-truth" of the source energy, which we then propagate to the subsatellite point to provide a "ground-truth" of the Poynting fluence in the EIWG in the vicinity relevant to trans-ionospheric transmission estimates. The VLF propagation in the EIWG, from the stroke to the subsatellite point, depends on the Long Wave Propagation Capability (LWPC) numerical model developed by the United States Navy (Pappert & Ferguson, 1986). The WWLLN data with approximate energy estimates will be referred to as "WWLLNae" data within text and figures to follow. The energy estimates provided by WWLLNae (Hutchins et al., 2012, 2013) are accompanied by estimated errors in the energy estimate. In this study, we accept energy estimates with estimated errors up to 50%. Combined with the fact that the method developed by Hutchins to estimate the far-field VLF energy flow in the EIWG relies on a number of simplifying approximations (Hutchins et al., 2012, 2013), we regard the estimated Poynting-fluence density at the subsatellite point as being *subject to factor-of-two uncertainty*. That is, the actual fluence density probably lies in the range from one-half, to twice, the estimated fluence density. Although this uncertainty is large, it will still allow us to identify trends in the trans-ionospheric transmission, and also to identify much larger variability associated with that transmission.

Besides using the LWPC numerical model in our estimate of VLF source energy for a stroke, we also use the LWPC to properly model how the signal attenuates as it propagates from the stroke location to the region of the subsatellite point. We rely on the LWPC twice: first, to assist in the calibration of the WWLLN array and second, to take a stroke whose source energy has been estimated, and then to estimate the Poynting-flux density in the EIWG in the vicinity of the subsatellite point. This second application of the LWPC will be described further in section 6 below.

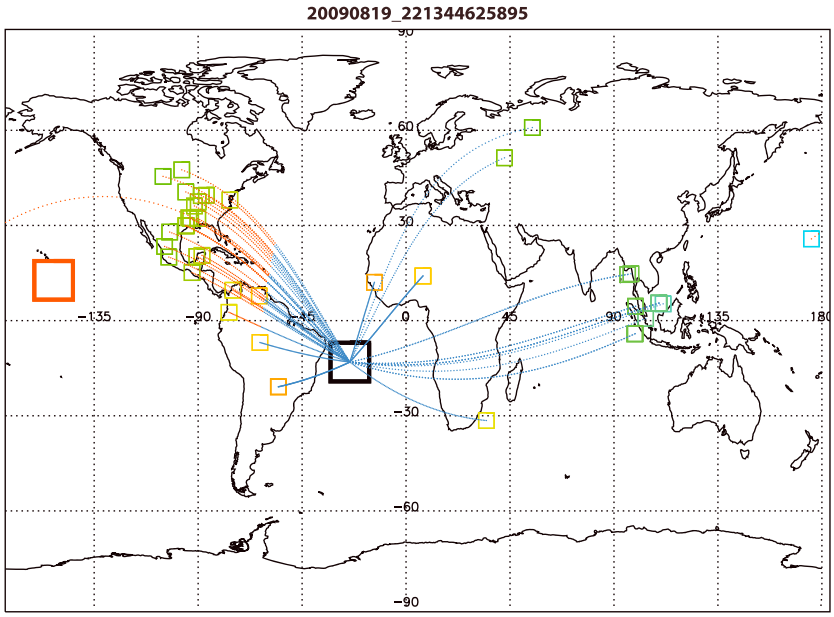

Figure 1. Map of Earth during one 12 s duration VEFI broadband recording on 19 August 2009, at approximately 22 UT. The large black square indicates the subsatellite location, the large red square indicates the subsolar point, and the small squares indicate WWLLNae lightning-stroke locations for strokes occurring during this particular record. The stroke locations are color-coded for great circle distance from the subsatellite point, with deep red = 0 km and deep blue = 20,000 km (the antipode). The great circle paths are also shown, color-coded for either sunlit (orange) or dark (blue) at *D*-layer height.

2.3. General Approach to Relating C/NOFS and WWLLN

Our approach to melding C/NOFS and WWLLNae data is to identify lightning strokes, which have been characterized (location, time, and source VLF energy) by WWLLN, and whose VLF waves are also detected by VEFI. Figure 1 shows an example. This is a global map covering the time window of one VEFI record (12 s duration) occurring on 2009 August 19 at around 22:13 UT. The large black square east of Brazil is the subsatellite point. The small squares are *all* the lightning-stroke locations that WWLLN provided during the 12 s time window. The color of the stroke symbol indicates the great circle arc-distance from the subsatellite point, ranging from 0 (deep red) to the antipode at 20-thousand km (deep blue). The subsolar point is the large red square over the Pacific. The great circle paths from the subsatellite point to each stroke are shown. The color denotes local daytime (solar zenith angle $<90°$) along the path in orange color, and local nighttime (solar zenith angle $>90°$) in blue color. This angle is reckoned at *D*-layer height.

VEFI pulses are automatically identified, using a method that has been thoroughly described by a previous publication (Jacobson et al., 2016). The key point is that whistler signals arrive at the recorder as highly dispersed in time. In order to identify pulses in the time domain, it is necessary to "dechirp" the signals so that they compress into narrow pulses. However, one does not know, in advance, the optimal dispersion strength to use in the dechirp (Jacobson et al., 2011). Thus, one needs to iteratively test different values of the dispersion strength, and then to select, as the "appropriate" dispersion strength, that value producing the narrowest pulses. On the other hand, there is no guarantee that the appropriate dispersion constant remains the same throughout the record, nor that it is single-valued even at the same time. The new method (Jacobson et al., 2016) largely overcomes those challenges. The method consists of the following steps:

1. A zero-padding is prepended to the entire record (typically 12 s duration).
2. The entire record, including the zero-padding, amounts to M time samples and is Fourier transformed to the frequency domain in one coherent fast Fourier transform.
3. A grid of N trial dispersion strengths to be used in dechirping is defined, in regular steps over the entire range likely to be seen in zero-hop whistlers.

Table 1
Database for This Study

	Statistic	Value	Notes
1	Date range of data	31 July 2009 to 28 March 2014	
2	Number of qualifying records	5547	Out of 20911 possible records
3	Cumulative number of detected VEFI whistlers in the qualifying records	1.21-million	
4	Cumulative number of located WWLLN strokes during the qualifying records	364-thousand	
5	Cumulative number of located WWLLN strokes during the qualifying records, with predicted Poynting-fluence-density in EIWG$>10^{-6}$ ($\mu J/m^2$) at subsatellite point	163-thousand	
6	Cumulative number of located WWLLN strokes during the qualifying records, with predicted Poynting-fluence-density in EIWG$> 10^{-6}$ ($\mu J/m^2$) at subsatellite point, and estimated source energy >2 times the estimated error	136-thousand	
7	Minimum (maximum) number of detected VEFI whistlers in any qualifying record	3 (1089)	
8	Minimum (maximum) number of located WWLLN strokes during any qualifying record	2 (183)	
9	Cumulative number of located WWLLN strokes with apparently coincident VEFI whistlers	118-thousand	46% erroneous (estimated) See Figure 2a
10	Cumulative number of detected VEFI whistlers in the qualifying records, with dechirped pulsewidth <15 samples	318-thousand	
11	Cumulative number of located WWLLN strokes with apparently coincident VEFI whistlers having pulsewidth <15 samples	58.8-thousand	27% erroneous (estimated) See Figure 2b
12	Cumulative number of located WWLLN strokes <5,000 km arc-distance from satellite, with apparently coincident VEFI whistlers having pulsewidth <15 samples	28.5-thousand	16% erroneous (estimated) See Figure 2c
13	Cumulative number of located WWLLN strokes with apparently coincident VEFI whistlers having pulsewidth <15 samples, with predicted Poynting-fluence-density in EIWG $>10^{-6}$ ($\mu J/m^2$) at subsatellite point, and estimated source energy >2 times the estimated error	19.0-thousand	

4. For each of the N trial dispersion strengths in the grid, the entire record is "dechirped" in the frequency domain, then reverse-Fourier-transformed back to the time domain. This returns a vector of M time samples. All N implementations of this step are stored in an M × N matrix.
5. Temporally sharp peaks (along the time axis $m = 1, 2, \ldots, M$) are sought in the M × N matrix, using several pulse-detection criteria.

The mere fact that VLF pulses are received by VEFI during the same 12 s epoch as the WWLLN-located strokes does not, however, mean that there is any correspondence between the two phenomena. To establish a correspondence, and to provide an estimate of the likelihood of false correspondence, we examine the time relationship between VEFI pulses and WWLLN strokes statistically, for the entire aggregate of 5,547 recordings included in our data set for this study (see Table 1). Figure 2 shows histograms of the corrected time differences between WWLLN strokes and VEFI pulse detections. By "corrected" we mean compensated for propagation delay and for ionospheric pulse dispersion (Jacobson et al., 2011). The uncertainty in this time-difference is partly controlled by the approximately 1 ms uncertainty in the onboard timing on C/NOFS (Jacobson et al., 2011), and more importantly, by an additional uncertainty of a few milliseconds incurred in the identification of VEFI pulses by the automated procedure (Jacobson et al., 2016).

Figure 2 shows the distribution of time differences, in bins of 1 ms width. Figure 2a shows a completely nonselected distribution of time-differences (dt) for all 1.21-million VEFI pulses and all 364-thousand WWLLN strokes occurring in aggregate during the records. At the center of the distribution is a peak, which is a signature of there being some level of true correlation. On the flanks of the distribution there is only random, or accidental, correlation, shown as a flat level, indifferent to delay. That random level is measured as 5,479 "accidents"/ms. The signature of some true correlation is seen in the range $-4 < dt < +6$ ms, shown by light vertical grey lines. There are 118,072 dt pairs within those central limits. Because we expect the accidental level to be indifferent to dt, we may estimate that there are likely to be about 54,790 accidents among the 118,072 dt pairs within those central limits. This is illustrated as the grey-shaded rectangle, whose top boundary is the continuation of the flank level across the "correlation zone." In other words, we estimate that 46% of the unselected dt pairs within the "correlation zone" are likely to be accidental, or false-positive correlations. This is an unacceptably high false-positive rate for inferring the properties of true correlations.

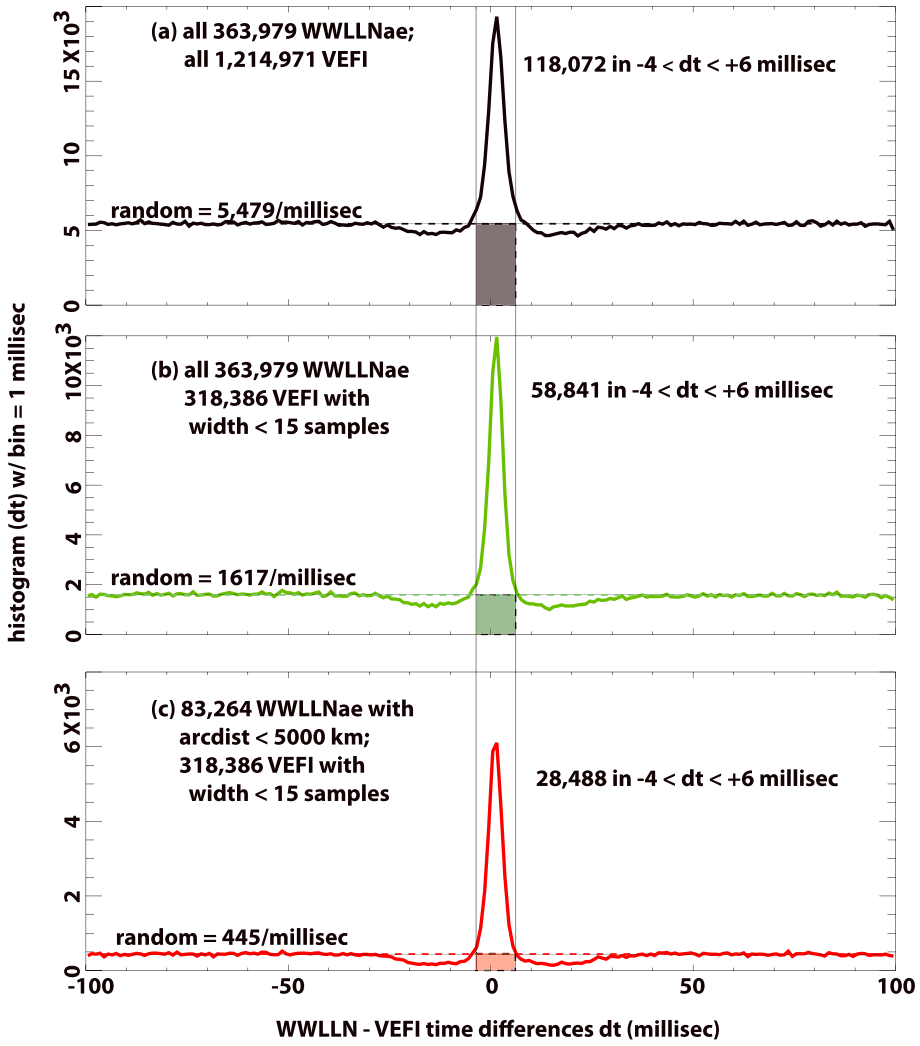

Figure 2. Histograms of time difference between propagation-corrected WWLLNae stroke time and VEFI pulse time, in bins of 1 ms. (a) All time differences, between all WWLLNae strokes and all detected VEFI pulses. (b) Same but with reduced set of VEFI pulses having temporal width <15 samples (0.47 ms). (c) Same but with both reduced set of VEFI pulses having temporal width <15 samples (0.47 ms) and reduced set of WWLLNae strokes no more than 5,000 km distant from the subsatellite point. The shaded rectangles are estimated random-coincidence levels (see text).

To lower the rate of false positives, we impose increasingly strong selection of what data we allow. It turns out that pulsewidth is in large part an inverse proxy for signal-to-noise ratio, as very weak pulses (relative to the noise) have systematically broader signatures, while very strong pulses have systematically narrower signatures. Figure 2b shows the first level of selection: We select for only those VEFI pulses whose energy width (Jacobson et al., 2016) is less than 15 VEFI samples (or 0.47 ms). This selects down to only 318-thousand VEFI pulses among the universe of 1.21-million VEFI pulses used in Figure 1a. The estimated false-positives (see the green-shaded rectangle in Figure 1b) now are down to ~16,170, while the overall number of *dt* pairs within those central limits is down to 58,841. Thus, merely selecting by pulsewidth has driven the false-positive rate down to 27%.

A further selection criterion, to seek a further lowering of the false-positive rate, is to require that the WWLLN locations be within some maximum arc-distance from the subsatellite point. Note that arc-distance, like pulsewidth, also serves as an inverse proxy for pulse signal-to-noise ratio. Choosing that arc-distance limit as 5,000 km (approximately one quarter of the distance to the antipode), we have limited the number of WWLLN strokes down to 83-thousand. Figure 2c shows the *dt* distribution for this limited set of WWLLN strokes and for the width-limited VEFI pulses. This lowers the false-positive rate to 16%.

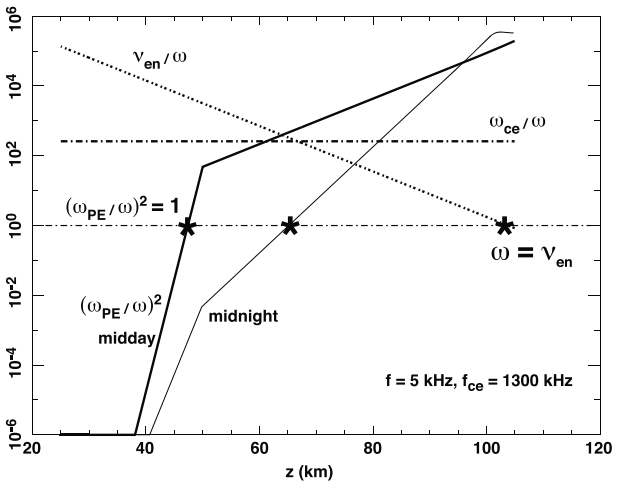

Figure 3. Profiles of typical midday and midnight exponential models of *D* layer, for wave frequency 5 kHz and electron gyrofrequency 1,300 kHz. See text for details.

The progression from no data selection (Figure 2a), then to one form of selection (Figure 2b), and finally to two forms of selection (Figure 2c) illustrates the truism: if one improves the quality of data by imposing selection criteria, then one ends up with less data. The limit on how far we choose to go in pursuing these selections depends on how much selected data are needed to allow adequate sampling of the independent variables. This is a trade-off with no single unique, perfect solution. Table 1 summarizes the data set, the selection criteria, and the effect of applying the selection criteria.

This comparison of WWLLN strokes with detected VEFI pulses is consistent with two observations:

1. Since WWLLN has less than 100% stroke-detection efficiency and tends to detect the stronger strokes and to miss the weaker strokes (Hutchins et al., 2012), it is expected that the weaker VEFI pulses would have fewer opportunities to be associated with a WWLLN ground-truth event. Therefore, by restricting the VEFI candidate pulses to only the narrowest (and therefore strongest) pulses, we improve the chance that there is a true WWLLN correlated stroke.
2. Also contributing to the problem with correlating broad (weak) VEFI pulses is that our automated algorithm for detection of pulses (Jacobson et al., 2016) errs on the side of creating false-positive detections. Thus, the weaker the VEFI pulse identified by our algorithm, the more likely it is to be just a feature in the noise, that is, a contrivance of the algorithm.

3. *D*-Region Control Over Coupling From Waveguide to Magnetosphere

Since we are comparing Poynting-fluence density at the satellite to that below the ionosphere, we need a model of the transionospheric propagation and losses. The path from the atmosphere to the inner magnetosphere goes through the *D* region, *E* region, and lower–*F* region ionospheres (Helliwell, 2006). Of these, the *D* region is the most important control on signal attenuation, in particular for near-grazing incidence, which is most pertinent to the coupling from waveguide modes in the atmosphere to the *D* layer. The *D* region's dominant role in signal attenuation is due to the exponentially decreasing value of the electron-neutral collision frequency, which at these altitudes greatly exceeds the electron-ion collision frequency. The collision-frequency's logarithmic derivative is approximately $-0.15\ \mathrm{km}^{-1}$ (see section 6.1 below), so that going higher than 105 km, into the upper *E* region and the *F* region, leads to relatively small collisional attenuation, compared to the attenuation suffered in the *D* region. The *D* region electron-density profiles are usually approximated by exponentials (Wait & Spies, 1964). Although exponentials do not capture the full complexity of real instantaneous profiles measured by rocket probes (Friedrich & Rapp, 2009), those complexities are highly variable in both space and time, and entirely unknown in real time along the actual path taken by these signals. Therefore, exponential profiles of electron density versus height are as good as we can find for this purpose, from a practical perspective.

Typical *D*-layer conditions in the exponential approximation are shown in Figure 3, assuming a wave frequency f = 5 kHz. The numerical values of the exponential-curve parameters are given below in section 6.1. The curves tilting upward to the right show the ratio squared of the plasma frequency ω_{pe} to the wave radian frequency ω, for typical midday (thick curve) and midnight (thin curve) conditions. The vertical axis is dimensionless. The dotted curve tilting downward to the right is the ratio of the electron-neutral collision frequency ν_{en} to the wave radian frequency ω. Note that the dynamics are heavily collisional ($\nu_{en} > \omega$) for f = 5 kHz in the *D* layer. Note also that the electron radian gyrofrequency ω_{ce} exceeds the collision rate ν_{en} in most of the *D* layer. Thus, the electrons are collisional but magnetized in much of the *D* layer for 5 kHz wave frequency. Under these circumstances, the wave partially couples from a (collisional) plasma wave to a (collisional) whistler wave near the altitude where the wave frequency equals the plasma frequency.

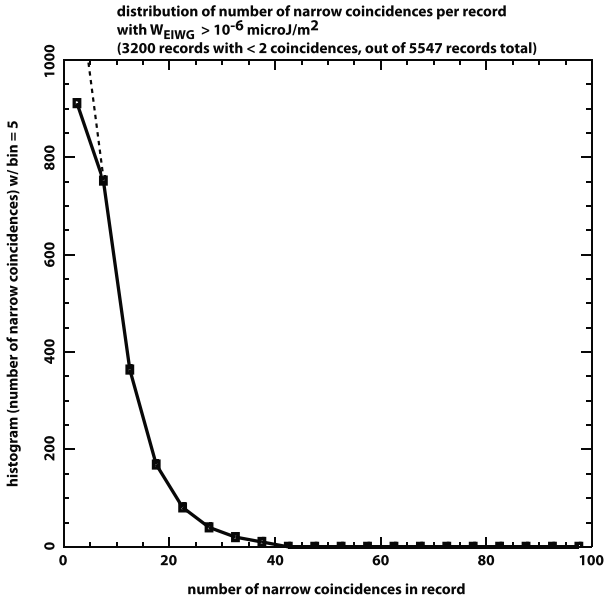

Figure 4. Distribution of number of narrow VEFI pulses detected during records. 3,200 (out of 5,547) have either 1 or 0 pulses—too few to contribute to the pair-difference results such as Figures 17 and 18 below. See text for details.

4. Poorly Predicted Sporadic Variability of Detectable Lightning-Related Whistlers

This section describes a negative finding, which is key to understanding our results: Most of the VEFI observing records are devoid of detected lightning-generated whistlers that can be associated with strokes located by WWLLN.

Relatedly, the occurrence of VEFI-detected whistlers is sporadic, that is, not just quantitatively but also qualitatively inconsistent. The number of VEFI-detected whistlers often varies radically between two records that would appear, on the basis of (a) contemporaneous lightning locations, (b) propagation conditions from the strokes to the subsatellite region, and (c) propagation conditions from the subsatellite region to the satellite, to be quite similar. Our expectation when we started this work had been that the transmission from the lightning stroke to the satellite would occur in a reasonably consistent manner, able to be predicted by careful application of both the LWPC model of the EIWG part of the propagation, and then of the full-wave model (Jacobson et al., 2009, 2010, 2012) of the upward coupling to a magnetospheric "zero-hop" whistler wave. At this time, however, we must acknowledge that the upward propagation through the lower ionosphere at these low magnetic latitudes is apparently subject to a sporadic-enhancement effect that is not predicted by the full-wave model (see Appendix A) of wave coupling through a perfectly laminar *D* layer. The remainder of this article will show the evidence.

During the observation period (from mid-2009 to early 2014) for this study, we had over 20-thousand "qualifying" data records for analysis. See Table 1 for details. The necessity for "qualifying" is that all three antennas must be operating, and the record must be free of gross malfunction (e.g., radio interference from attitude-control system operation). Of these 20-thousand "qualifying" data records, however, only 5,547 pass two additional requirements necessary to merit further analysis in this study: First, as described above in section 2.1, we require the wave electric field to be approximately orthogonal to the geomagnetic background field; that is, $<E^2_{par}>/<E^2_{perp}>$ must not exceed 0.015. Second, as described in detail in previous publications (Jacobson et al., 2011, 2014, 2016), we require that the Langmuir probe indicates a sensible absence of density fluctuations. In fact, these two requirements each eliminate substantially overlapping cohorts of records, because we find that the principal cause of failing the first criterion is that there are small-scale density irregularities, revealed by the Langmuir probe, causing the record to be dominated by strong lower-hybrid wave activity of the sort seen for several decades by earlier workers (see references and results in Bell & Ngo, 1988, and Bell & Ngo, 1990). Whenever VEFI records contain visible lower-hybrid wave activity, we find that it is impossible for the whistler-detection algorithm to identify discrete whistlers among the noise.

The remaining 5,547 records (see Table 1) are then automatically analyzed to identify, characterize, and catalog discrete whistler pulses (Jacobson et al., 2016). We catalog 1.2-million pulses in this manner (line 3 in Table 1). Of these, only 318-thousand meet the narrow-pulsewidth criterion (<15 samples, i.e., 0.47 ms pulsewidth), which we shall favor in deriving quantitative results (line 10 in Table 1). Of these 318-thousand pulses, only 59-thousand have probable association with WWLLN-located lightning strokes. Knowing from WWLLN a probable source location and source VLF energy, it is possible to model the Poynting-fluence density in the EIWG in the subsatellite region using an LWPC calculation (see section 6.1 below). We finally require the modeled EIWG Poynting-fluence density to be $>10^{-6}$ (μJ/m^2), as it will become apparent (see section 6.2 below) that any weaker lightning disturbances are usually below our limit of detection anyway.

The coincident pulses selected in this manner are the input to Figure 4, which shows the observed distribution of number of selected pulses per record. The pulses are selected to have width <15 samples and to have predicted Poynting-fluence density $>10^{-6}$ (μJ/m^2). The bins are occupancy per record, in steps of 5 pulses per record. First, we note that of the 5,547 records, a majority (3,200) have fewer than 2 selected

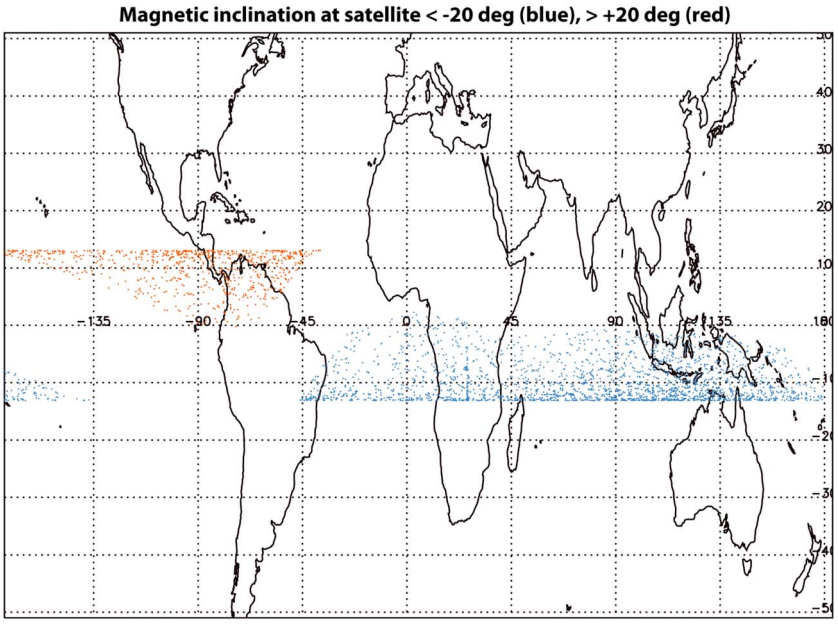

Figure 5. Subsatellite locations of VEFI records with magnetic inclination (at the satellite) $> +20°$ (red) and $< -20°$ (blue). Locations are not shown on this map if the magnetic inclination is in the range -20 to $+20°$.

coincident pulses; that is, they have either zero, or only one, selected coincident pulse. If we include the cases of one selected coincident pulse, then the lowest bin is extended upward (see dashed line, going offscale.)

5. Sampling of Significant Geophysical Variables

Since our conclusions will be based on statistical inference, we must reveal the sampling of various geophysical variables by the data set. These geophysical variables include, for example, magnetic inclination at the satellite, separation range from the lightning source to the subsatellite region, solar zenith angle, and signal magnetic azimuth of arrival at the subsatellite region.

5.1. Sampling of Magnetic Inclination

Magnetic inclination has long been understood to be one of the most robust controls over VLF transmission through a laminar *D* region. The C/NOFS near-equatorial orbit, with 13° orbital inclination, has allowed us to monitor VLF transmission within a range of magnetic inclinations from roughly -50 to $+40°$. On the basis of laminar, full-wave calculations of VLF transmission, it is expected that very little VLF energy is predicted to be transmitted upward through the *D* region at the lowest inclinations (say, -15 to $+15°$) (see, e.g., model results in Figures 8 and 9 of Starks et al., 2008). We apply our own model to model this effect in Appendix A below.

Figure 5 maps the subsatellite positions of records whose magnetic-inclination magnitude at the satellite is $>20°$. The lowest-magnetic-inclination records (magnitude less than 20°) are not shown. The positive-inclination records (red points) are concentrated in the Americas, where the magnetic equator is most displaced southward, while the negative-inclination records (blue points) are to be found over the Indian Ocean and the Maritime Continent, where the magnetic equator is most displaced northward. This illustrates how the C/NOFS orbit, despite an orbital inclination of only 13°, can sample magnetic-latitude magnitudes twice as great, albeit not at the same longitude.

As mentioned in section 4 above, the magnetic inclination by itself does appear to exercise some control over the incidence of lightning-whistler pulses identifiable by our automated approach. We need identifiable pulses to subject to ground-truthing and further analysis. To show this bias, we now group VEFI records into bins of magnetic inclination, with each bin 9° wide, ranging from -50 to $+40°$. Figure 6 graphs bin-medians of the population of detected pulses within records. The bin-median is the median of the populations of all records *lying in that bin*. Figure 6a does this for all detected pulses, while Figure 6b is only for narrow (width < 15 samples) pulses. Recall that only narrow pulses are most likely to have trustworthy WWLLN

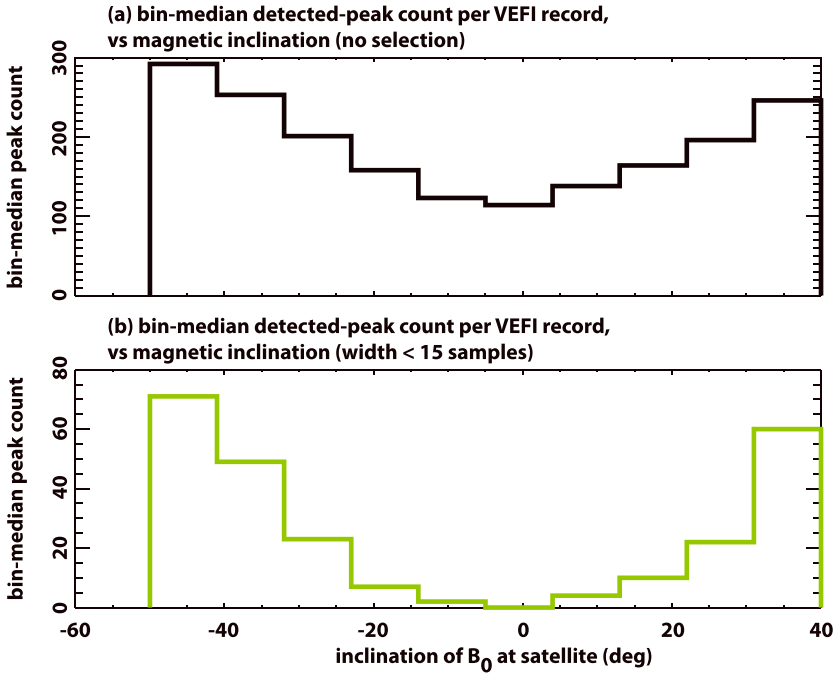

Figure 6. Median number of VEFI pulses per record, versus magnetic inclination at the satellite. (a) No selection of VEFI pulses. (b) Only narrow VEFI pulses (<15 samples).

ground-truth (see Figure 2 above). Evidently very low magnitudes of magnetic inclination partially suppress the bin-median detected population, and this is most dramatic for the restricted case of narrow pulses. We caution that this result is only for detected pulses that are identified and detected by our algorithm. The magnetic-inclination control over raw whistler power (whether or not identified and detected as discrete pulses) versus magnetic dip angle may be related but is not directly tested here. As for our data set's sampling of magnetic inclination, the important conclusion to be drawn from Figure 6b is that most of the narrow (high signal-to-noise ratio) pulses available for ground-truthing and subsequent analysis lie away from the magnetic equator, that is, at magnetic inclinations $> +20°$ and $< -20°$.

5.2. Sampling of Arc-Distance From Lightning to Subsatellite Point

If lightning occurred uniformly over the surface of Earth, then we would expect that the distribution of arc-distance, ρ, from the subsatellite point to contemporaneous WWLLNae strokes would be controlled only by the area element of available Earth surface at that arc-distance. That area element varies as $\sim\sin(\rho/R_e)$, where R_e is the Earth's radius. Of course, the assumption going into this scenario is not even approximately correct. Figure 7 shows various arc-distance distributions seen in the data. Let us focus first on the (topmost) dark solid black curve, which is the distribution versus arc-distance of available WWLLNae stroke locations. These are "available" in that they occur contemporaneously with a record. Near the ends of the domain (0 km, and the antipode at 20-thousand km), the distribution is controlled most by the expected area-element factor $\sin(\rho/R_e)$. However, apart from the ends, the area-element factor does not control the arc-distance distribution. That is because the global distribution of lightning, far from being uniform, is peaked at low latitudes and even more so is peaked over land regions, both continental and insular (Christian et al., 2003). The annular area elements are not homogenously filled with lightning.

In Figure 7, the black dashed curve is the distribution of arc-distance to those strokes that are apparently correlated to VEFI pulses (regardless of width). Subsequently, this class of VEFI pulses will be called simply "coincident." This curve reflects the detectability bias toward shorter-range paths. Below about 1,000 km range, essentially *all* the WWLLNae strokes have a VEFI correlation. Out to 5,000 km, the correlation rate is >50%. At greater distances, this falls to the order of 20%. The green curve is similar, but using only those VEFI pulses with width <15 samples. The green curve is most relevant to our data selection for analysis later on. It indicates that the detection of lightning pulses by VEFI in these observations maintained 10% or better detection

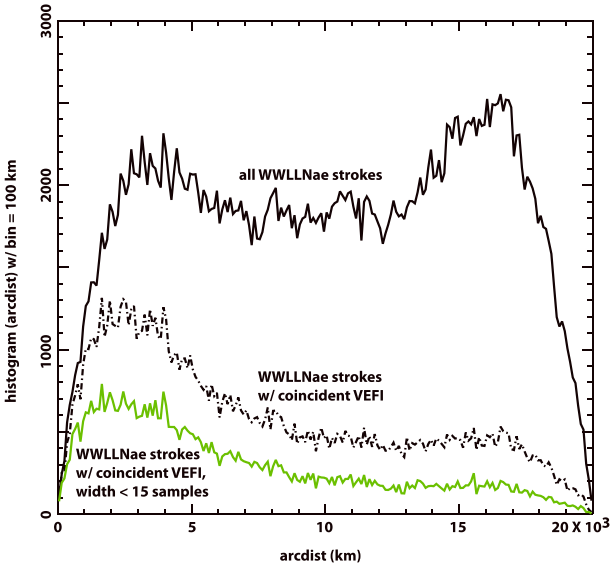

Figure 7. Distribution of great circle arc-distance from WWLLNae stroke locations to subsatellite point. The black solid curve is for all WWLLNae strokes contemporaneous with VEFI records. The black dashed curve is for coincidences. The green curve is for narrow coincidences.

efficiency out to global range (i.e., the antipode). Subsequently, this class of VEFI pulses will be called simply "narrow coincident."

5.3. Sampling of Solar Illumination

By design, the bulk of our observing records were under conditions of darkness at the satellite (solar zenith angle >90°) or only slightly above the horizon. This was to allow minimum loss due to *D*-layer dissipation. However, the global range of detection (see Figure 7 above) causes us to have less control over the solar zenith angle at the stroke location. Figure 8 shows the solar zenith-angle distributions at (a) the subsatellite point and (b) the stroke location. The black solid curves are for all contemporaneous WWLLNae strokes, with or without VEFI correlation. The black dashed curves are for only coincidences. The green curves are for narrow coincidences. Figure 8a confirms the observing plan for having the satellite in darkness during most burst recordings. In Figure 8b, the black solid curve for zenith angle at the stroke location (all contemporaneous WWLLNae strokes) is controlled by Earth-surface area-element variation at the extremes (near 0° and 180°). The correlation distributions (black dashed curve and green curve) increase toward darker conditions at the stroke location, as a fraction of all WWLLNae strokes, up to about 130° solar zenith angle (or 40° depression angle). This variation is related to the increase of Earth-ionosphere waveguide attenuation with increased illumination of the *D* layer. We describe in section 6 below our method of estimating the waveguide attenuation so as to predict the VLF Poynting-flux density in the waveguide near the subsatellite point.

Another way of examining the control by the *D* layer over waveguide losses is to plot distributions of the day-lit fraction of great circle paths (from stroke to subsatellite point). We do this by calculating the instantaneous solar zenith angle at a grid of points along each great circle path. The day-lit fraction of that path is the fraction of the distance for which the solar zenith angle is less than 90°. Figure 9 shows these distributions. The upper black curve is for all WWLLNae strokes. The black dashed curve is for only coincidences. The green curve is for narrow coincidences. The green curve indicates that the more day-lit is a path, the less likely is that path to yield a WWLLNae correlation with a narrow VEFI pulse. That is consistent with the idea that a sunlit *D* layer causes more waveguide attenuation, and that more attenuation causes the pulses to become smaller compared to the noise, which leads to increased pulsewidth. To some extent, though, the effect may also be due to the fact that longer paths tend to be more likely to have greater sunlit fraction, because the satellite typically is in local nighttime.

5.4. Sampling of Magnetic Propagation Azimuth at Subsatellite Point

The magnetic propagation azimuth of arrival at the subsatellite point (of the great circle path to the area of the subsatellite point) affects both the waveguide attenuation (Hutchins et al., 2013) and the efficiency of upward coupling to magnetospheric whistlers (Jacobson et al., 2012). C/NOFS and VEFI data have already been used at least to identify azimuth sensitivity of this sort (Burkholder et al., 2013). This dependence on azimuth is due to the anisotropic dielectric properties of a magnetized plasma. Due to the tendency of most lightning to occur over land and insular regions at low latitudes, and to the near-equatorial position of C/NOFS, we expect the availability of great circle azimuths of arrival to peak in the zonal directions. Figure 10a shows the magnetic-propagation-azimuth-of-arrival distribution for all contemporaneous WWLLNae strokes occurring during VEFI records. These are the lightning strokes *available* for possible VEFI detection, whether or not the latter occurs. The zonal elongation of the distribution is consistent with the fact that relative to the C/NOFS near-equatorial position, there is more lightning available in the east and west than in the north and south. The color progression of the bin symbols codes the magnetic propagation azimuth at the subsatellite point and will be used in subsequent graphics (Figures 12 and 14): from deep red at +180°, counterclockwise to deep blue at −180°. The asymmetry between eastward and westward lobes in Figure 10a is a peculiarity of the location of the satellite relative to contemporaneous lightning locations.

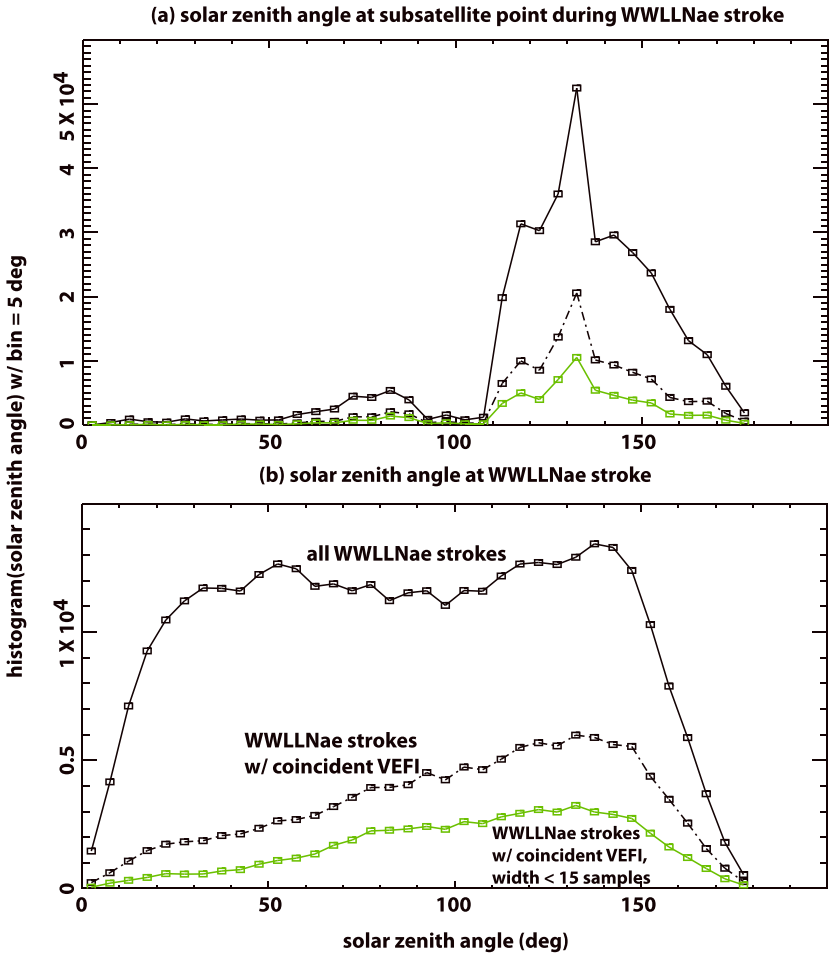

Figure 8. Distribution of solar zenith angle at *D*-layer height. (a) At subsatellite point. (b) At stroke location. The black solid curve is for all WWLLNae strokes contemporaneous with VEFI records. The black dashed curve is for coincidences. The green curve is for narrow coincidences.

Figure 10b is similar but is limited to WWLLNae strokes that are correlated to narrow VEFI pulses (width $<$ 15 samples). Note that compared to the available-strokes distribution in Figure 10a, the narrow-pulse-correlation distribution in Figure 10b noticeably favors the available lightning whose VLF waves in the EIWG propagate toward the magnetic east, compared to the magnetic west. This is qualitatively consistent with previous studies of ground-to-ground, over-the-horizon VLF propagation (Hutchins et al., 2013; Pappert & Hitney, 1988). However, the behavior in Figure 10b is also influenced by other factors, including the anisotropy of *D*-layer upward penetration, so that we may not claim that Figure 10b is a definitive confirmation of the previous studies on zonal asymmetry.

6. Inferred Upward Transmission Through the *D* Layer

6.1. Calculation of Path Attenuation in the Earth-Ionosphere Waveguide

The inference of approximate upward transmission of VLF through the *D* layer of the lower ionosphere relies on knowing, if only approximately, the wave strength immediately below the *D* layer, that is, in the EIWG, in the vicinity of the subsatellite point. This wave strength sets the "incident" wave in the upward transmission through the *D* layer and into the ionosphere. That is, we need to know the "incident" wave's strength in order to infer, from the "transmitted" wave's strength at the satellite, a "transmission coefficient."

Each stroke's source-energy estimate in the WWLLNae energy-estimate product is accompanied by an error estimate. This estimate is based on formal parameter estimation made possible by requiring more

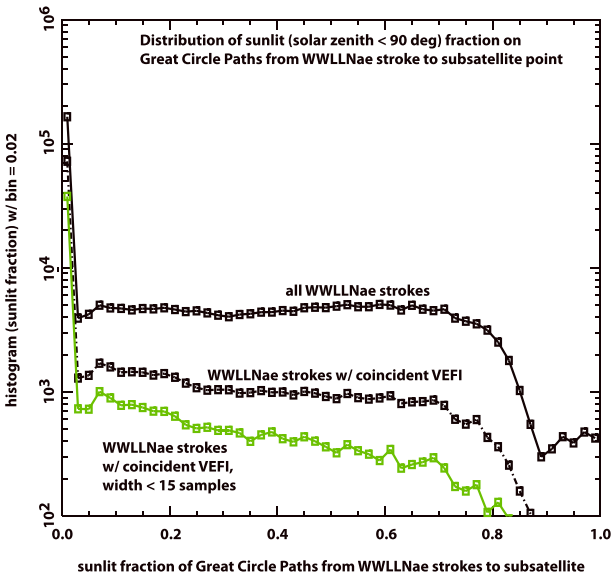

Figure 9. Distribution of fraction of great circle path that is sunlit at *D*-layer height. The black solid curve is for all WWLLNae strokes contemporaneous with VEFI records. The black dashed curve is for coincidences. The green curve is for narrow coincidences.

data inputs (stations) than the minimum required (Hutchins et al., 2012), that is, requiring positive degrees of freedom in the fit to source energy. In the data selection for the work reported here, we use only those WWLLNae stroke solutions having at least three degrees of freedom. Within this selected set, we further select for only those strokes whose estimated energy error is less than half the estimated source error. Imposing that pair of selection criteria yields the 364-thousand WWLLNae strokes used in this study (see Table 1). Note that this estimate is admittedly very approximate, even in terms of estimated random errors. The systematic errors are additive to the random errors.

For each WWLLNae stroke, we use LWPC code to obtain day and night estimates of the waveguide transmission from the stroke location to the subsatellite point. We assume that the electron density n_e varies exponentially versus altitude z, viz. $n_e = n_0 \exp(p(z\text{-}h_p))$. Here n_0 is a reference density, p is a logarithmic derivative, and h_p is a reference height. Analogously, we assume that the electron collision frequency ν_{en} varies as $\nu_{en} = \nu_0 \exp(-q(z - h_q))$. The midday (midnight) parameters are $n_0 = 3 \times 10^8$ m^{-3}, $p = 0.15$ km^{-1} (midday) or 0.35 km^{-1} (midnight), $h_p = 70$ km (midday) or 85 km (midnight), $\nu_0 = 5X10^6$ s^{-1}, $h_q = 70$ km, and $q = 0.15$ km^{-1}. The electron-neutral collision rate is the same both night and day. By contrast, the electron density profile differs markedly between day and night, extending lower in altitude and being shallower in slope during the day than during night.

The first estimate of waveguide transmission is with a midday *D*-layer model, while the second is with a midnight model. Each estimate is implemented for a grid of discrete frequencies within our VLF passband. Each estimate applies its respective *D*-layer model uniformly along the great circle path. The ground conductivity, of course, is the same for the two estimates, but does vary along the path according to LWPC's atlas. The waveguide transmission is tabulated assuming a hypothetical, continuous-wave 100 kW source located at the lightning stroke. The calculation tabulates the resulting root-mean-square wave electric field in the center of the waveguide at the subsatellite location, assuming the monochromatic, 100 kW continuous source. The archived quantity is 20 times the logarithm (base 10) of the field in units of μV/m. To convert to a broadband transmission, we average the archived logarithmic field over the frequencies of our VLF passband. This frequency-averaged quantity is called the "reference electric field." For each stroke, there is one reference electric field for midday conditions, and one for midnight conditions. The systematic approximations here are additive to the random errors in the parameter estimation.

We illustrate in Figure 11 the reference electric field estimates for ~81-thousand strokes lying at short range (<5,000 km) from the subsatellite point. The blue scatter points are for midnight, while the red are for midday *D* layer. The continuous curves above the scatter points represent a "toy" model in which there is no lossy attenuation (at either the ground of the *D*-layer waveguide boundaries), and the total, azimuth-integrated power is conserved versus range. The figure serves to show the importance of lossy attenuation even at short range. The scatter points in Figure 11 are spread (vertically) due to profound differences in the contribution of the ground (to waveguide attenuation) between different great circle paths, and due to profound differences caused by propagation magnetic azimuth.

As mentioned earlier, the EIWG has an attenuation that varies significantly versus propagation magnetic azimuth. We show that in Figure 12 for all 364-thousand WWLLNae strokes' great circle paths, for (a) a midday *D* layer and (b) a midnight *D* layer. The color is used to code propagation magnetic azimuth at the subsatellite point. The color scale is the same as in Figure 10. In particular, the yellow and orange points are for propagation toward the eastward quadrant, while the blue and green points are for propagation toward the westward quadrant. Note that, in general, the propagation magnetic azimuth varies along the Great-Circle path; shown here is only the magnetic azimuth *at the subsatellite point*, which is the endpoint of the wave path in the EIWG.

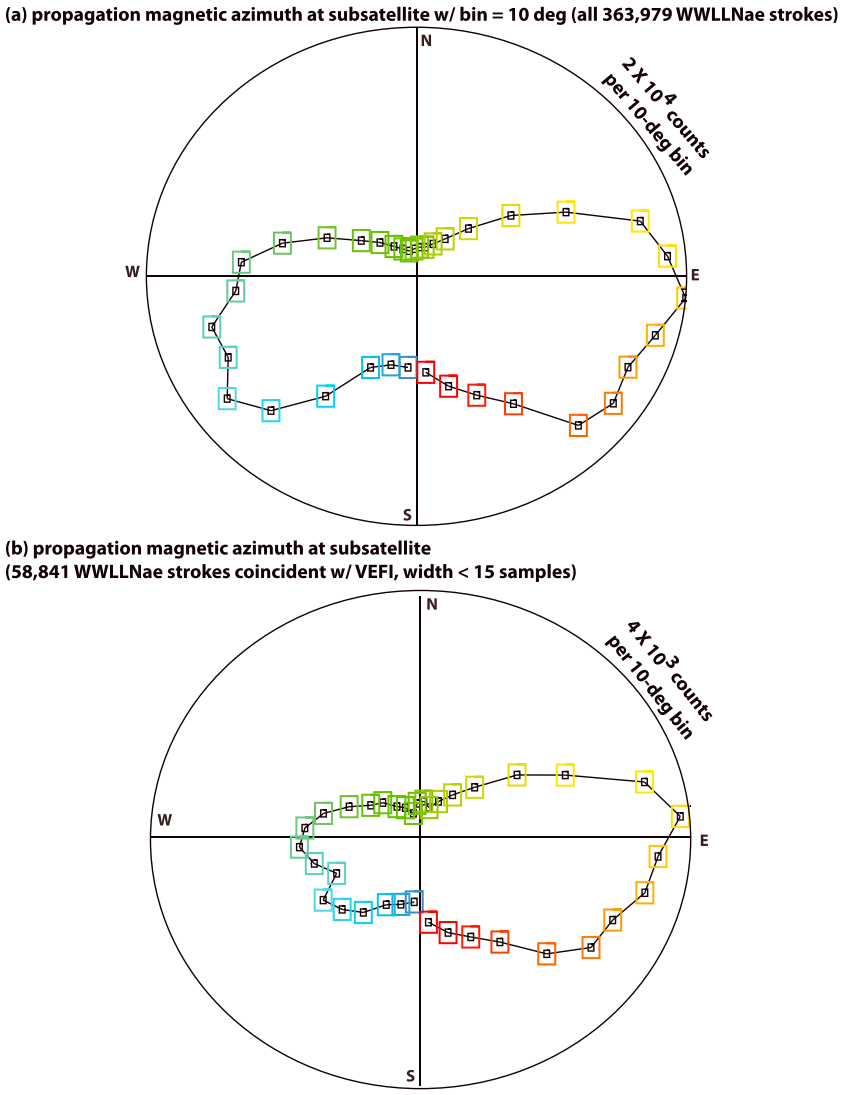

Figure 10. Distribution of great circle-path magnetic propagation azimuth at the subsatellite point. (a) All WWLLNae strokes contemporaneous with VEFI records. (b) Narrow coincidences. The color indicates magnetic azimuth and will be used again in Figures 12 and 14 below.

6.2. Approximate Calibration of VLF Poynting-Fluence Density in the Earth-Ionosphere Waveguide

The following two steps exploit the reference-wave-field calculations described above, to predict the time-integrated Poynting-flux density, that is, Poynting-fluence density, in the EIWG at the subsatellite point.

First, we take a weighted average of the midday and midnight reference-field parameters. The weighting of the midday parameter is the fraction of the great circle path for which the Sun is above the horizon, while the weighting of the midnight parameter is the fraction of the path for which the Sun is below the horizon. The two weights add up to unity. This is a crude way of estimating the overall logarithmic transmission of the path under the actual illumination conditions at the time of the stroke, but limiting our calculations to just two extremes of the *D*-layer illumination. We call this weighted average the "blended" reference field. This approach has been presented previously (Hutchins et al., 2012, 2013), where it was found that the error incurred by this simple weighting procedure could corrupt the energy-attenuation estimates by 20% to 25%.

Second, we take the estimated source energy (from the WWLLNae product) for each stroke, and use the blended reference field for that stroke's path and time, to predict the Poynting-fluence density in the EIWG

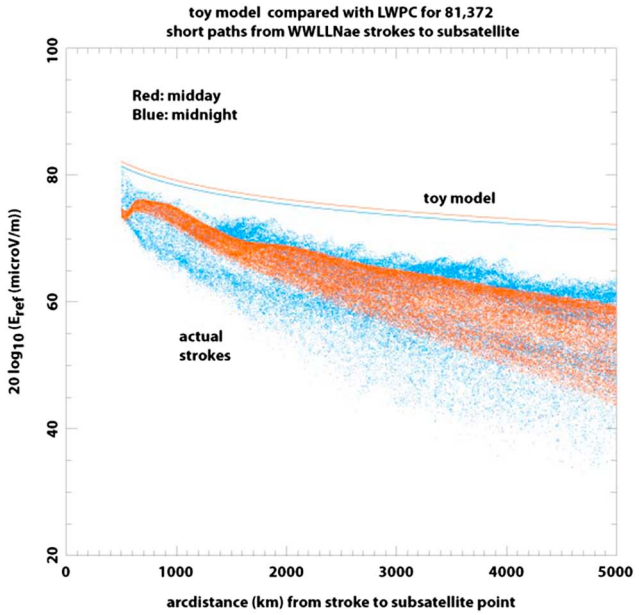

Figure 11. Assuming a constant 100 kW transmitter at the stroke location, this shows the modeled root-mean-square electric field of the transmitted wave at the subsatellite point, for only those WWLLNae strokes contemporaneous with VEFI records and <5,000 km distant. The blue marks midnight *D* layer; the red marks midday *D* layer. The solid curves are for a toy model assuming a perfectly conducting ground and a perfect-conducting reflector at the *D* layer. Vertical axis logarithmic. See text for details.

under the satellite due to each stroke. This will be suitable for comparison to the Poynting-fluence density at the satellite.

Figure 13 shows the resulting distributions of estimated Poynting-fluence density in the EIWG under the satellite. This is a log-log plot. The horizontal bins are in constant increments (=0.5) of the logarithmic variable $\log_{10}${EIWG Poynting-fluence density ($\mu J/m^2$)}. The dark black solid curve is for all 364-thousand WWLLNae strokes. The dashed black curve is for coincidences. The green solid curve is for narrow coincidences. The red curve is similar to similar to the green curve but is limited to strokes located less than 5000 km from the subsatellite point. Subsequently, this class of VEFI pulses will be called simply "short-range, narrow coincidence."

The progression downward through these four curves in Figure 13 causes selective exclusion of the lower-fluence part of the distribution ($<10^{-6}$ $\mu J/m^2$), while the higher-energy flank ($>10^{-4}$ $\mu J/m^2$) is relatively unaffected. Let us compare Figure 13 with Figure 2. The three curves in Figure 13 pertaining to VEFI-concurrent strokes (dashed black, green, and red) correspond to the same selection criteria as in Figures 2a–2c, respectively. Those three cases in Figure 2 illustrate the effectiveness of data selection in reducing the rate of "false" correlations. As summarized in Table 1, that rate reduces from 46% (black curve in Figure 2a), through 27% (green curve in Figure 2b), to 16% (red curve in Figure 2c). Returning to Figure 13, then, we see that the false correlations are largely generated when attempting to correlate VEFI pulses with WWLLNae strokes whose fluence density under the satellite is in the lower-energy part of the distribution ($<10^{-6}$ $\mu J/m^2$). Our understanding of this is as follows: The algorithm for removing the dispersion of, and then identifying, VEFI pulses (Jacobson et al., 2016) has been tuned to maximize the chances of detecting pulses, rather than to minimize the chance of false detections. That is, in the continuum from "false negatives" to "false positives," our detection algorithm is relatively "open," that is, tuned toward allowing a significant number of false positives. It appears therefore that the VEFI pulses correlated with WWLLNae strokes having weak fluence under the satellite are highly corrupted by false pulses (false on the VEFI side, not the WWLLN side). Thus, a prudent step to insulate this study from including false pulses is not to include VEFI "pulses" correlated with WWLLNae strokes having weak fluence density under the satellite ($<10^{-6}$ $\mu J/m^2$). The implication is that overall, 10^{-6} $\mu J/m^2$ might be the practical floor on EIWG VLF fluence density for successful VEFI detection of an upward coupled whistler within the ionosphere.

6.3. Observed Upward "Transmission Coefficient" Through the Ionosphere

For each detected VEFI pulse (Jacobson et al., 2016), we can infer the Poynting-flux density from the wave electric field, the wave polarization (Jacobson et al., 2014), and the ion composition from CINDI (Heelis et al., 2009). We integrate the Poynting-flux density versus time to get the Poynting-fluence density of the integrated pulse, within the receiver bandwidth. Figure 14 shows a log-log scatter plot of Poynting-fluence density inferred from VEFI and CINDI at the satellite, on the vertical axis, versus Poynting-fluence density underneath the ionosphere at the subsatellite point, on the horizontal axis. The color stands for propagation magnetic azimuth, as in Figures 10 and 12. The two cases are (a) coincident VEFI/WWLLNae pairs with the VEFI pulsewidth <15 samples and (b) further selection for the arc-distance from the stroke to be less than 5,000 km. The diagonal dashed black line is the equality line. The dark-black curve is the "binned median," representing the median of the vertical values, for all points lying in regular bins on the horizontal axis. Figure 14 is a core result of our work and requires several detailed explanations:

1. Estimates of either Poynting-fluence density, both in the EIWG and at the satellite, are subject to *order-of-magnitude errors*. Errors in the estimated Poynting-fluence density in the EIWG accrue from the 50% uncertainty in the WWLLNae source-energy estimate, convolved with the inadequacies of the LWPC propagation prediction, convolved with the extreme simplification of the *D*-layer model fed into the LWPC. Errors in the estimated Poynting-fluence density at the satellite accrue from the errors in the

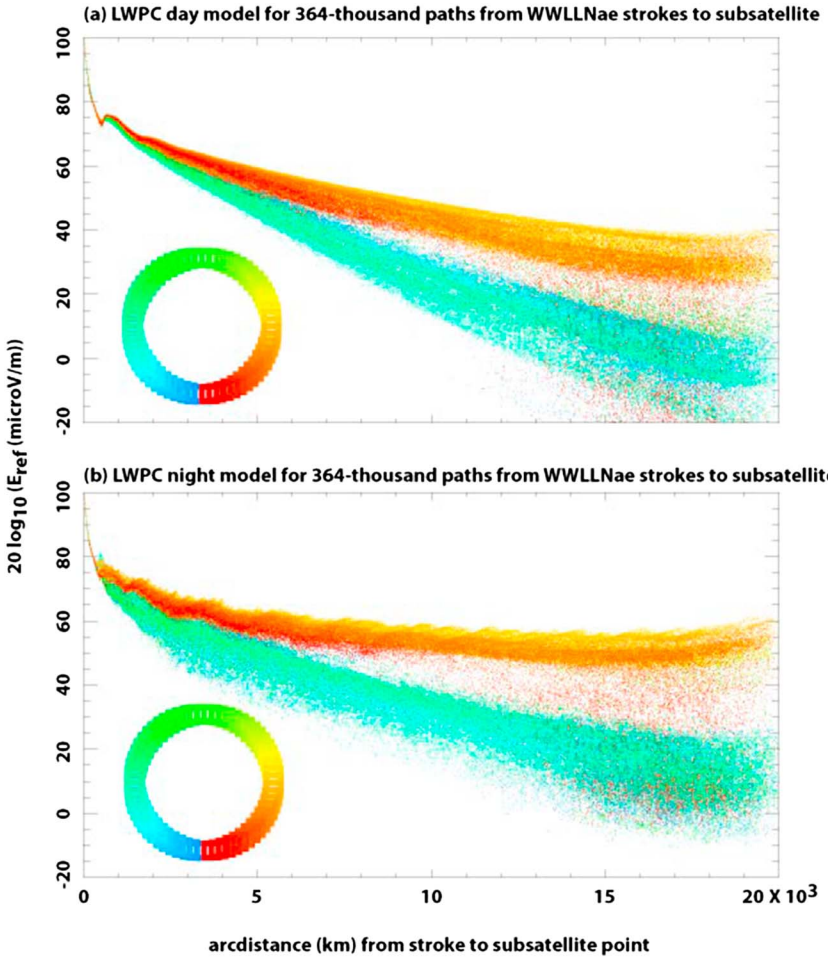

Figure 12. Similar to Figure 11 but for the actual paths and sunlit fractions of all WWLLNae strokes contemporaneous with VEFI records. Here the color indicates propagation magnetic azimuth at the subsatellite point. (The color key is shown in the color wheel and is consistent with Figure 10 above.) Note that the magnetic azimuth at the subsatellite point is not identical to the magnetic azimuth elsewhere on the path. The discrepancy between red/orange and blue/green points is consistent with the well-known favoring of eastward propagation in the Earth-ionosphere waveguide.

wavevector retrieval, convolved with the errors in the index-of-refraction retrieval, convolved with the errors in the electric-field retrieval (Jacobson et al., 2014).

2. The data points appearing in the scatter plots are only for *detected VEFI events* with WWLLNae concurrence. However, the majority of WWLLNae strokes produce no detectable VEFI pulse, and therefore do not appear in Figure 14. This suggests that the data points in Figure 14 are a minority showing enhanced "transmission" compared to the majority of WWLLNae strokes. Thus, Figure 14 shows the systematic transmission of a subset of lightning strokes only. Figure 14 does not describe the overall transmission, only that of an aberrant minority.
3. Given the enormous (order-of-magnitude) random errors in both the abscissa and ordinate values of the data points, we pay particular attention to the trend curves for the binned medians. For EIWG Poynting-fluence density $>10^{-5}$ ($\mu J/m^2$), the binned-median curves show a trend of linear transmission, with transmission coefficient (for energy) in the range 0.01 to 0.1. However, for EIWG Poynting-fluence density $<10^{-6}$ ($\mu J/m^2$), the binned-median curves show a floor at between 10^{-7} ($\mu J/m^2$) and 10^{-6} ($\mu J/m^2$) in the at-satellite Poynting-fluence density. This is consistent with the statement that VEFI, armed with our detection algorithm, is incapable of detecting "real" pulses accompanying WWLLNae strokes for which the EIWG Poynting-fluence density is below 10^{-6} ($\mu J/m^2$). What is detected at these low incident energies is mainly spurious, false-positive VEFI pulses, hovering near the detection threshold.

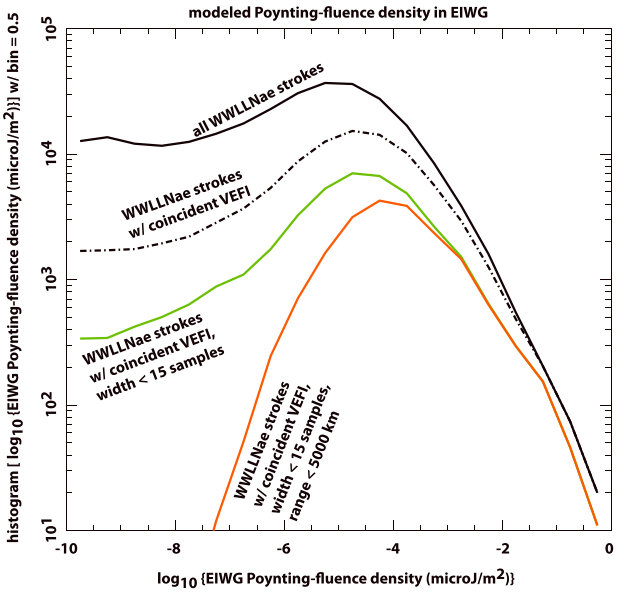

Figure 13. Distribution of modeled Poynting-fluence density in Earth-ionosphere waveguide under the satellite. Log-log. The black solid curve is for all WWLLNae strokes contemporaneous with VEFI records. The black dashed curve is for coincidences. The green curve is for narrow. The red curve is for close, narrow coincidences. The bin-size is 0.5 in the logarithmic abscissa. The model of Poynting-fluence density combines the WWLLNae source-energy estimate, plus the LWPC propagation calculations. See text for details.

Summarizing, for incident pulses with Poynting-flux density $>10^{-5}$ (μJ/m^2) in the EIWG at the subsatellite point, most of the time VEFI detects nothing. However, in a minority of cases, VEFI detects a whistler with Poynting-flux density that is 1 or 2 orders of magnitude smaller than the incident pulse. There is slight color-separation, indicating that the transmission ratio might be marginally higher for magnetic-westward propagation than for magnetic-eastward propagation. However, the scatter in the detected/incident ratio is very large (see Figure 14), so this asymmetry is not well established by our data. See earlier observations (Burkholder et al., 2013).

The data summarized in Figure 14 suggests that in the minority of cases where detectable transmission through the ionosphere occurs, the detected energy transmission ratio is in the range 0.01 to 0.1. Compared to model predictions (see Appendix A and Table A1 below), the detected energy transmission is orders of magnitude greater than expected from a full-wave calculation of propagation through a laminar *D*-layer ionosphere. From this discrepancy, and from the fact that only a minority of cases show detectable transmission, we suspect that the detected transmission, during the minority of records when it occurs, is due to a sporadic process that is not described by a laminar-ionosphere model. Additionally, the data of Figure 14 are consistent with the observation that the VEFI "detection" system would not be able to see such faint signals as are predicted by the laminar-*D*-layer model. That is, the only reason that *some* lightning-generated whistlers were detected at C/NOFS for these low latitudes is that a nonlaminar process must have occurred to allow sporadic penetration at a level much stronger than the laminar model predicts.

As mentioned two paragraphs earlier, Figure 14 suggests that the ionospheric transmission may be anisotropic, with west-going waves having higher transmission than east going waves. However, the effect is overwhelmed by the noise (scatter) within the data cloud. In order to examine this anisotropy more robustly, we now bin the data into propagation-azimuth bins, and within each bin, we tabulate the median of the logarithmic transmission. This is shown in Figure 15. Figure 15a shows this for all of the data, regardless of magnetic inclination at the satellite. The radial direction shows the logarithm of transmission, in the negative domain. That is, greater radius means greater attenuation. The guide rings go from transmission of 10^{-1} (innermost ring). Clearly, east going waves are more attenuated than are west going waves, in terms of transmission through the ionosphere. The populations in each azimuth bin, which determine the random noise in the median, are evident in Figure 10 above. The lowest-population bin (due-northward) has about 500 members. The highest-population bin (just north of due-eastward) has about 4,000 members. Figure 15's lower panel repeats this polar diagram, but selecting for distinct extremes of the magnetic inclination at the satellite: (b) negative inclination $< -20°$ and (c) positive inclination $>+20°$. We see that the different extremes of magnetic inclination modulate the location of the lobe of azimuth anisotropy in the logarithmic transmission. For negative inclination at the satellite, the maximum attenuation occurs for SE going waves, while for positive inclination, the maximum attenuation occurs for NE going waves.

We emphasize that the presentation of trans-ionospheric transmission (attenuation) in Figure 15 presupposes that the EIWG-propagation predictions based on LWPC are correct. It is possible that the apparent anisotropies of trans-ionospheric transmission are actually aliasing anisotropic errors in the LWPC predictions of the wave electric fields in the EIWG, below the ionosphere. We are not able to rule-out that possibility.

6.4. Additional Details Regarding Magnetic-Inclination Controls Over Event Detection

Earlier (see Figure 6, in section 5.1 above) we showed that when the satellite was near the magnetic equator, the yield of detected VEFI pulses was greatly suppressed. This observation would be broadly consistent with the reduction of laminar-ionosphere VLF transmission as the magnetic-inclination magnitude approaches

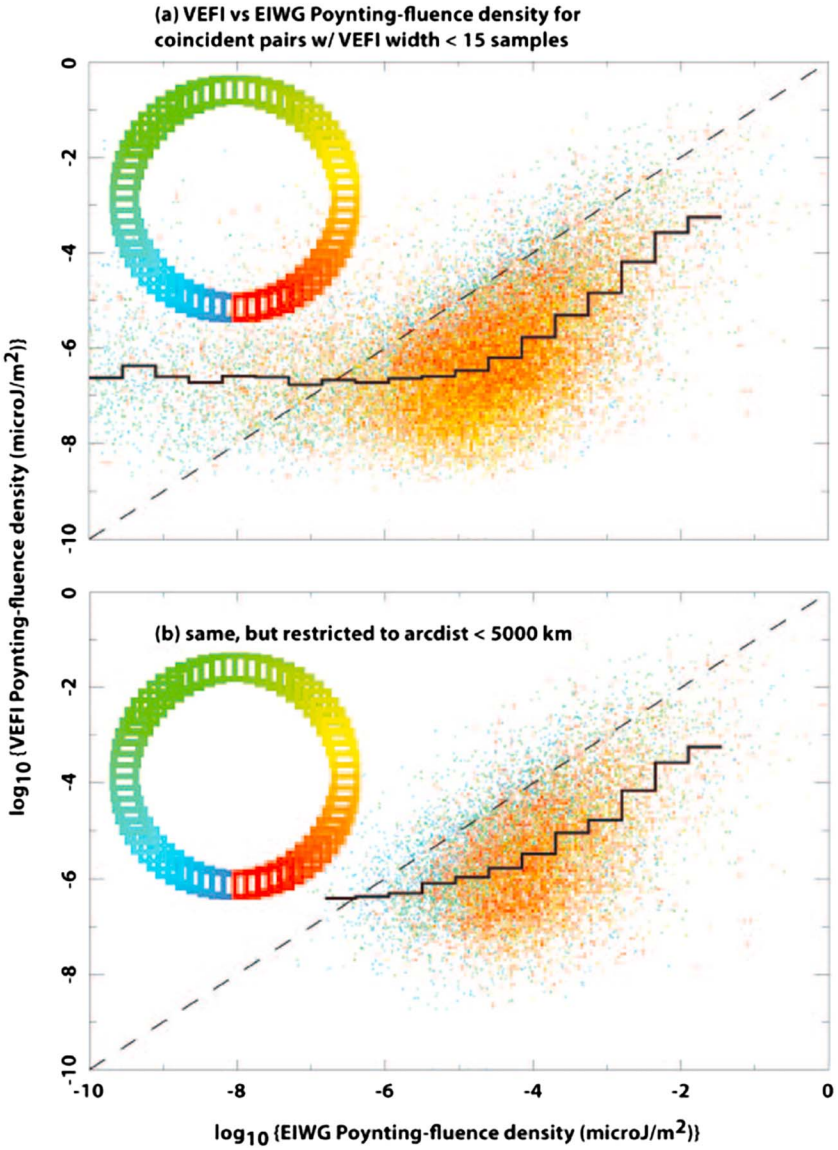

Figure 14. Scatter plot of *measured* Poynting-fluence density at satellite (vertical axis) versus *predicted* Poynting-fluence density at subsatellite point in Earth-ionosphere waveguide (horizontal axis.) Here the color indicates propagation magnetic azimuth at the subsatellite point. (The color key is shown in the color wheel and is consistent with Figure 10 above.) The dashed line is the equality line. The heavy black curve shows bin medians of the scatter points' ordinate value. (a) Includes only those WWLLNae strokes with narrow-pulse (<15 samples) VEFI coincidence. (b) Similar but further restricted to strokes that are <5000 km distant.

zero, for either full-wave (Starks et al., 2008) or sharp-boundary (Helliwell, 2006) models. On the other hand, we have shown (see section 6.3 above) that a laminar-ionosphere transmission model does not appear to account for our results. We see detectable transmission of lightning-generated VLF in only a minority of records, and when we do, the transmission is orders of magnitude greater than predicted by a full-wave model (see Appendix A). Thus, the lightning-generated whistlers we detect appear only to occur sporadically. We discuss in section 6.5 below why *D*-layer irregularities are implicated.

There are two approaches to use VEFI-detected VLF pulses to examine the effect of magnetic inclination at the satellite. The first approach is to tally the rate of coincidence of VEFI pulses to available WWLLNae strokes, within bins of magnetic inclination. The second approach is to examine, for those VEFI pulses reliably associated with a WWLLNae stroke, the ratio of the Poynting-fluence density at the satellite to the predicted Poynting-fluence density at the subsatellite point. Figure 16 contrasts these two approaches.

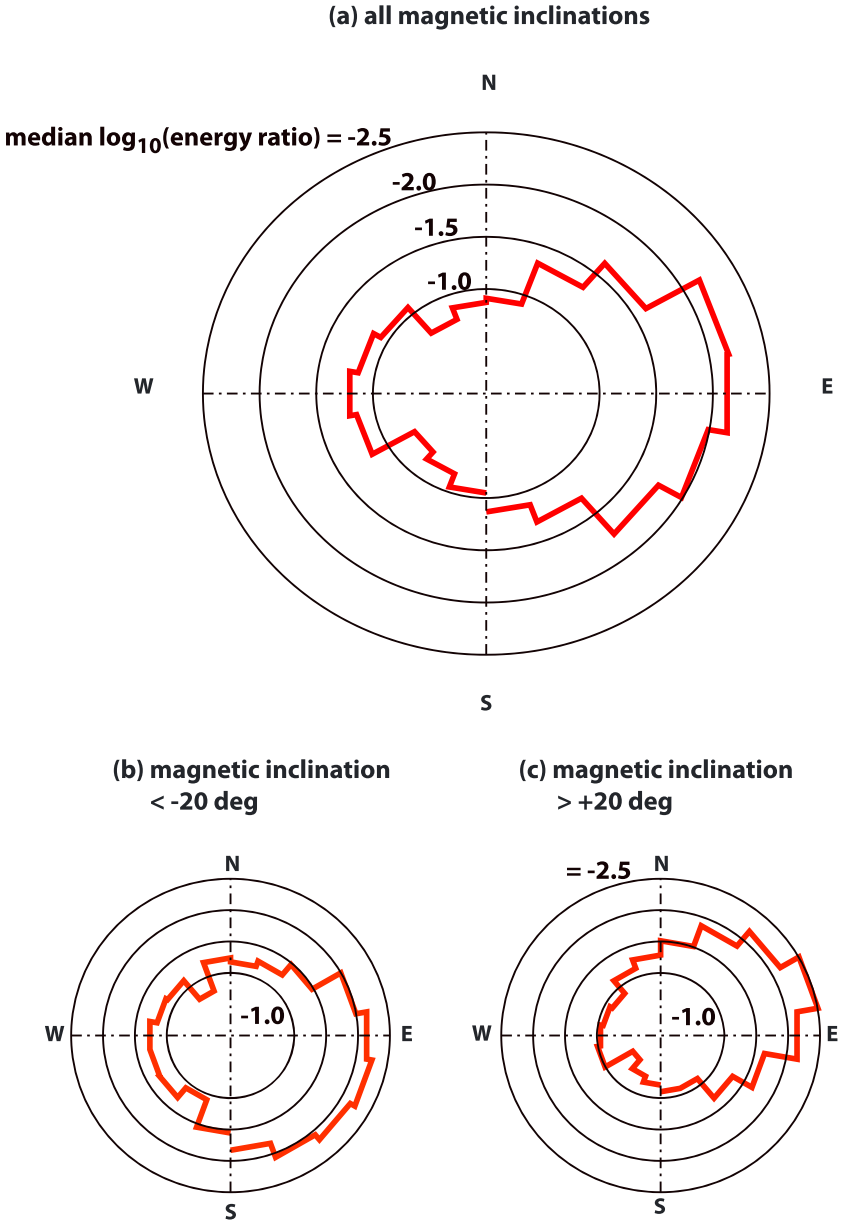

Figure 15. Bin-median logarithmic transmission ratio versus magnetic propagation azimuth at subsatellite point. Includes only close, narrow coincidences. Larger radius on the polar display indicates greater attenuation (smaller transmission), as the radius is proportional to a negative value of logarithm. (a) Unrestricted by magnetic inclination. (b) Restricted to magnetic inclination (at satellite) $< -20°$. (c) Restricted to magnetic inclination (at satellite) $> +20°$.

The WWLLNae strokes considered are only those with predicted Poynting-fluence density at the subsatellite exceeding 10^{-6} ($\mu J/m^2$). Earlier (in relation to Figures 13 and 14) we concluded that this is the threshold below which there is a very low rate of WWLLNae association with a VEFI pulse. Figure 16a graphs the VEFI-WWLLNae coincidence fraction versus magnetic inclination at the satellite. The overall appearance seems to be consistent with Figure 6 above. (Recall that the earlier figure displayed the number of VEFI pulses per magnetic-inclination bin, without regard to coincidence). Figure 16b graphs the bin-median logarithmic transmission ratio versus magnetic inclination at the satellite. Surprisingly, the lowest bin-median transmission occurs in the midrange of negative inclinations, not at the magnetic equator. We are unable to explain this. The behavior in Figure 16b) is unlike that expected from predictions based on a laminar *D*-layer transmission model, for which we would expect a minimum at the magnetic equator.

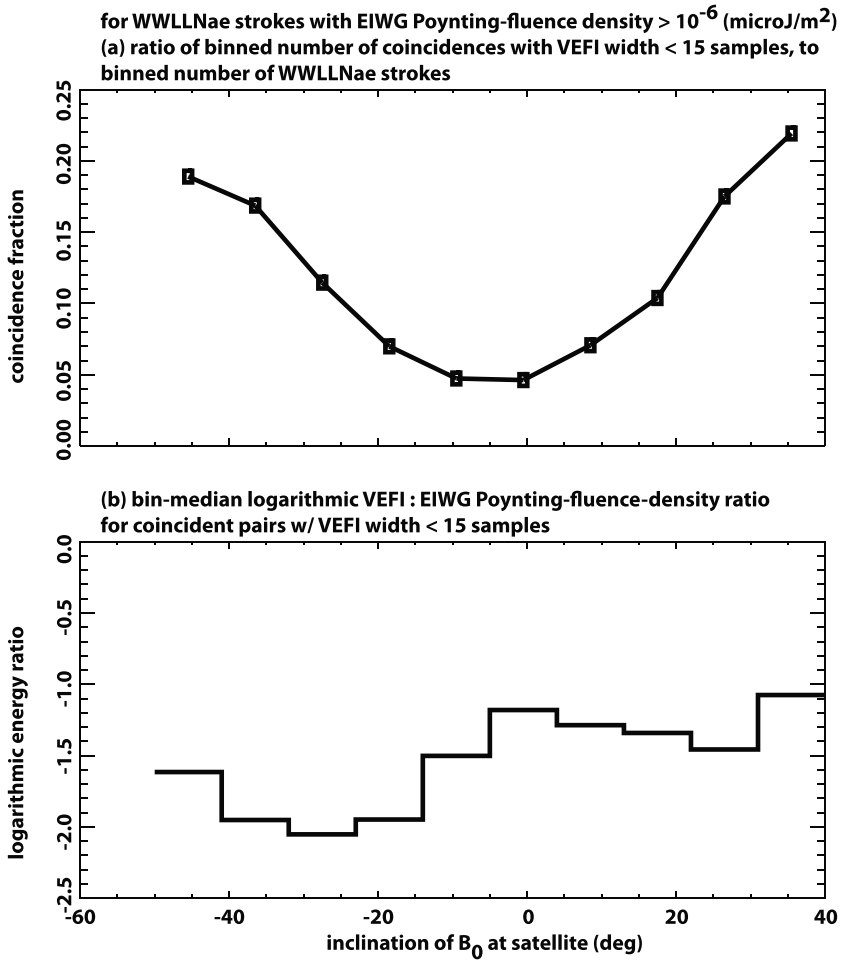

Figure 16. Variabilities of observed transmission ratio versus magnetic inclination at the satellite, for only VEFI pulses with narrow (< 15 samples) width. (a) "Correlation ratio": number of narrow VEFI coincidences divided by number of contemporaneous WWLLNae strokes with modeled Poynting-fluence density $>10^{-6}$ μJ/m^2 in the EIWG. The ratio is calculated within bins of magnetic inclination. (b) Bin-median logarithmic transmission ratio. The median is calculated within bins of magnetic inclination.

6.5. Evidence for Role of Spatial Irregularities in Enhancing D-Layer Transmission

So far, we have invoked spatial irregularities simply because the observed *D*-layer transmission occurs only sporadically, and when it does, at a greatly enhanced level compared to predictions from a laminar-*D*-layer transmission model. Now we present more compelling evidence to implicate spatial irregularities in the *D* layer. Since the satellite passes in the upper *F* region (>400 km altitude), and since VEFI records are accepted for this analysis only when the plasma-density irregularities at the satellite are undetectable (Jacobson et al., 2011, 2016), the transmission-enhancing irregularities must be at the *D* layer but not mapped, as "flutes" or "ducts," to the satellite. At any rate, the oblique-whistler raypaths from the *D* layer to the satellite are not exactly along field lines (Helliwell, 2006), so it is not expected anyway that there would be a detailed connection between a *D*-layer irregularity and observed plasma structures at the satellite. Moreover, the *D* layer is far too low, that is, too collisional, for upward electrostatic mapping of *D*-layer irregularities to the topside to be expected (Farley, 1959).

C/NOFS moves along its orbit at about v_{sat} ~ 7.5 km/s. The Doppler shift of slowly developing irregularities converts them from "DC" to apparent finite-frequency. Therefore, sensors of local quantities aboard C/NOFS observe temporal variation of those quantities, with apparent radian frequencies given by $\omega = k_{par}$ v_{sat}, where k_{par} is the irregularity wavenumber parallel to the orbit. Let us consider the logarithmic transmission ratio. As already seen (Figure 14), this statistic is extremely noisy, or scattered. Could the scatter

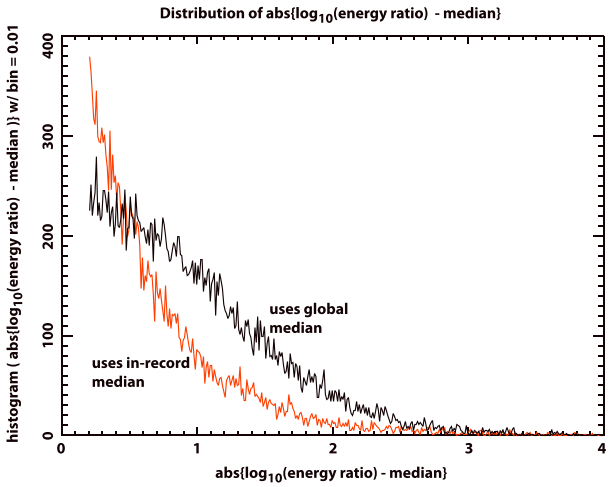

Figure 17. Distribution of logarithmic transmission ratio (energy ratio) absolute deviation from median. The black curve indicates that median is global median from all records. The blue curve indicates that median is separately calculated in each record. See text for details.

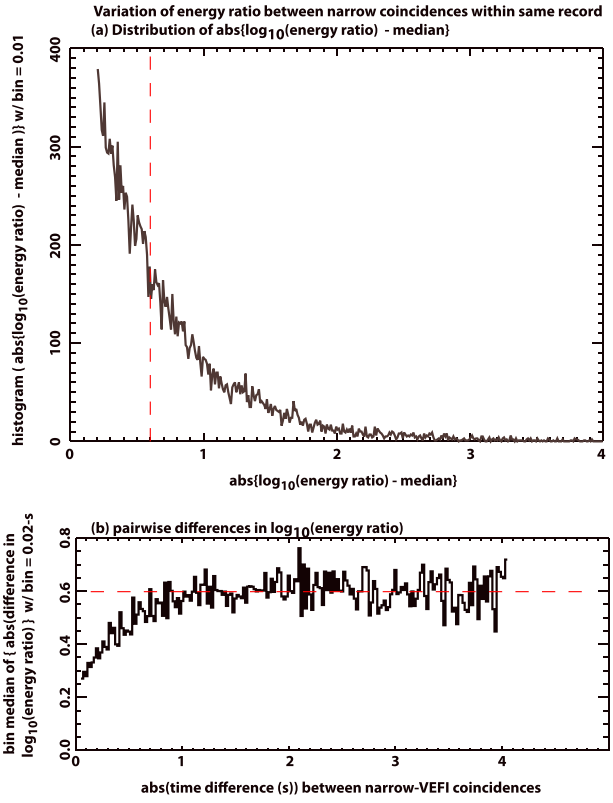

Figure 18. (a) Distribution of logarithmic transmission ratio (energy ratio) absolute deviation from per-record median. The dashed line shows the median absolute deviation from the median. (b) Pairwise differences in the logarithmic transmission ratio (energy ratio), versus time lag between the pair of measurements. Bin-size is 0.02 s. The dashed red line shows asymptote.

be controlled, partially or totally, by the *D*-layer irregularities? As noted earlier, VEFI records are extremely diverse in their yield of VEFI detected whistlers normalized to the number of available WWLLNae strokes. Consider the absolute variability of the logarithmic energy-transmission ratio, relative to its median. Figure 17 shows the distribution of the ratio, relative to both a global median (black curve) and a within-record median (red curve). Using the in-record median causes dramatically less scatter, that is, absolute deviation of the ratio from the median ratio, compared to using the global median. This is equivalent to saying that the transmission behavior is quite irreproducible between records. Records are separated by minutes to days. Taking 100 s as a minimum separation, that would be 750 km, minimum, of satellite progress along its orbit, and equivalently, of the upward propagating ray slicing through the *D* layer. Thus, whatever causes the record-to-record variability in transmission is effectively incoherent over an along-orbit scale of 750 km.

Figure 18a repeats the distribution shown in Figure 17's red curve, that is, for an in-record median. The vertical dashed line shows the median, which is ~0.6. This is the median absolute departure of the logarithmic transmission from the in-record median.

Within a record, which is ~12 s duration, we can examine the transmission's temporal correlations from 0 to 12 s, corresponding to spatial correlations from 0 to 90 km separation along the orbit. To do this, we make a table of all pairs of VEFI narrow, WWLLNae-correlated events within common record. That is, for each such event within a record, we tabulate all the pairwise differences in logarithmic transmission, between that one event and all other events within the record. We repeat this for each event within the record, and for all records. Figure 18b shows the bin-median of absolute difference between pairs of logarithmic-transmission, versus absolute time difference. The time-difference bin is 0.02 s. The distribution becomes increasingly noisy at larger separations, because the pair occupancy is monotonically falling with larger separation. Therefore, the abscissa is terminated at 4 s, rather than 12 s (the record duration). We see that the pairwise differences in logarithmic transmission start (at zero time difference) at a value near ~0.2, and then rise, over ~1 s of temporal separation, to an asymptotic value of ~0.6. The halfway point during the rise is at about 0.5 s, corresponding to a spatial separation of 3–4 km.

In summary, two repeated observations of the logarithmic transmission, in the limit of very short time (space) separation between the measurements, have a median absolute difference of 0.2. We identify this as the irreducible random error in the determination of the transmission using our technique, which is not perfect. As we let the temporal separation between the members of the pair increase, the median absolute difference in logarithmic transmission undergoes an increase, or equivalently the two measurements decorrelate further, with a "decorrelation time" ~0.5 s. After ~1 s, the asymptotic level is reached. The asymptotic level, 0.6, is 0.4 greater than the irreducible random error (0.2) seen at zero time separation between measurements. We attribute this extra 0.4 of temporal (spatial) decorrelation to *D* region irregularities with scales on the order of a few kilometers. Such irregularities could scatter and otherwise modify the VLF transmission through the *D* layer, relative to the rather low levels predicted by a laminar-*D*-layer model.

7. Conclusions

We have used joint WWLLNae and LWPC predictions of the lightning-generated energy flow in the EIWG, plus measurements of energy flow in the detected whistler wave correlated with that whistler, to infer an effective transmission coefficient through the ionospheric *D* layer at low magnetic latitudes. In most records, the WWLLNae strokes are poorly correlated with detected whistlers, but in a minority of records, there is substantial correlation. When there is correlation, the inferred transmission ratio is orders of magnetic greater than predictions based on a full-wave model based on a laminar *D* layer.

The sporadically occurring enhanced transmission of VLF through the *D* layer appears to decorrelate over a temporal separation of 0.5 s, corresponding to 3–4 km of distance along the satellite path. This is probably associated with kilometric irregularities in the ionospheric *D* layer, which is the main limitation on trans-ionospheric transmission.

Irregularities, by producing horizontal gradients of the *D* region medium, would allow a form of duct propagation, which is more efficient at transmission (Helliwell, 2006) than is the laminar solution (for the latter, see Appendix A). At this time, there is substantial evidence from other fields for *D*-layer irregularities. For example, it has been shown that the ubiquitous occurrence of sprite discharges at *D*-layer heights implies the existence of electron-density irregularities (Liu et al., 2012). From a different area of work, measuring bottomside reflectivity of the *D* layer using VLF and low-frequency radio waves, it has been inferred that the *D*-layer electron-density is frequently modulated spatially by the passage of acoustic-gravity waves originating in the troposphere (Lay & Shao, 2011; Lay et al., 2014).

Appendix A

A.1 Full-Wave Model of Energy Coupling

The full-wave reflection, transmission, and absorption of VLF plane waves in the lower ionosphere have been studied by several computational models (see, e.g., Lehtinen & Inan, 2009; Piggott et al., 1965; Pitteway, 1965; Starks et al., 2008). We shall use a plane wave, harmonic, linear model (Jacobson et al., 2009, 2010) based on the first full-wave scheme, which originated half a century earlier (Piggott et al., 1965; Pitteway, 1965), which we call the "Pitteway" scheme after its originator. The model has performed well at predictions of the dispersive, anisotropic reflection of broadband lightning-generated VLF from the ionosphere (Jacobson et al., 2012). That study validated the model's predictions using detailed measurements of reflection of lightning VLF signals from the ionosphere. The calculation of reflection requires simultaneous solution of the VLF transmission through the ionosphere; the two are intimately coupled (Pitteway, 1965). If the calculated transmitted solution were wrong, then so would the reflected solution be wrong, and vice versa. This gives us some confidence that our model, which has been validated for reflection (Jacobson et al., 2012), is likely to be equally valid for transmission.

The Pitteway scheme identifies two wave solutions, the "dominant solution" and the "penetrating solution." Both solutions must be calculated correctly for the prediction of reflected waves, while only the penetrating solution contributes to the transmitted wave. The two solutions are matched to the incident wave in the EIWG as a boundary condition. Each solution is elliptically polarized. By contrast, the incident wave from the lightning sferic is linearly polarized. Only about half of the incident wave energy is coupled into the penetrating solution; the rest couples into the dominant solution. The ionospheric energy-transmission coefficient is the ratio of the penetrating-solution's upward Poynting-fluence density at the top of the calculation, compared to the penetrating-solution's upward Poynting-fluence density at the base of the ionosphere. Therefore, the model energy-transmission coefficient overstates the total transmission (using the entire incident wave) by about a factor of 2.

The wavefields of the penetrating solution are calculated below altitude 105 km using the full-wave solver, with simultaneous solution of Maxwell's equations with the anisotropic, collisional dielectric tensor of the lower ionosphere (Jacobson et al., 2009, 2010). By the time it reaches 105 km altitude, the wave has become a whistler robustly satisfying the ray-optic (WKB) approximation. Moreover, most of the lossy attenuation of the penetrating solution between the EIWG and the satellite occurs in the full-wave region (below 105 km) due to high electron-neutral collisionality in the *D* layer (Piggott et al., 1965; Pitteway, 1965). To characterize the model transmission to the satellite, we take the ratio of the

Table A1
Modeled Ratio (at f = 10 kHz) of Ionosphere/EIWG Poynting-Fluence Density, Averaged Over Magnetic Azimuth of Arrival

Angle of incidence (deg)	Dip = 35°	Dip = 30°	Dip = 25°	Dip = 20°	Dip = 15°	Dip = 10°
60	6.9×10^{-3}	3.8×10^{-3}	1.8×10^{-3}	6.3×10^{-4}	1.6×10^{-4}	2.2×10^{-5}
70	3.4×10^{-3}	1.9×10^{-3}	8.7×10^{-4}	3.1×10^{-4}	7.9×10^{-5}	1.3×10^{-5}
80	1.0×10^{-3}	5.9×10^{-4}	2.7×10^{-4}	9.5×10^{-5}	2.4×10^{-5}	4.2×10^{-6}
82	6.7×10^{-4}	3.9×10^{-4}	1.8×10^{-4}	6.3×10^{-5}	1.6×10^{-5}	2.7×10^{-6}
84	3.9×10^{-4}	2.3×10^{-4}	1.1×10^{-4}	3.7×10^{-5}	9.3×10^{-6}	1.6×10^{-6}
86	1.8×10^{-4}	1.1×10^{-4}	5.0×10^{-5}	1.7×10^{-5}	4.3×10^{-6}	7.3×10^{-7}

Poynting-fluence density at the satellite to the Poynting-fluence density below the *D* layer. Thus, the denominator in this ratio is the incident plane wave's Poynting-fluence density below the ionosphere, in the EIWG, directed along the incident wavevector, while the numerator is the Poynting-fluence density at the satellite, directed along the Poynting vector at the satellite. We note that these two directions are in general different.

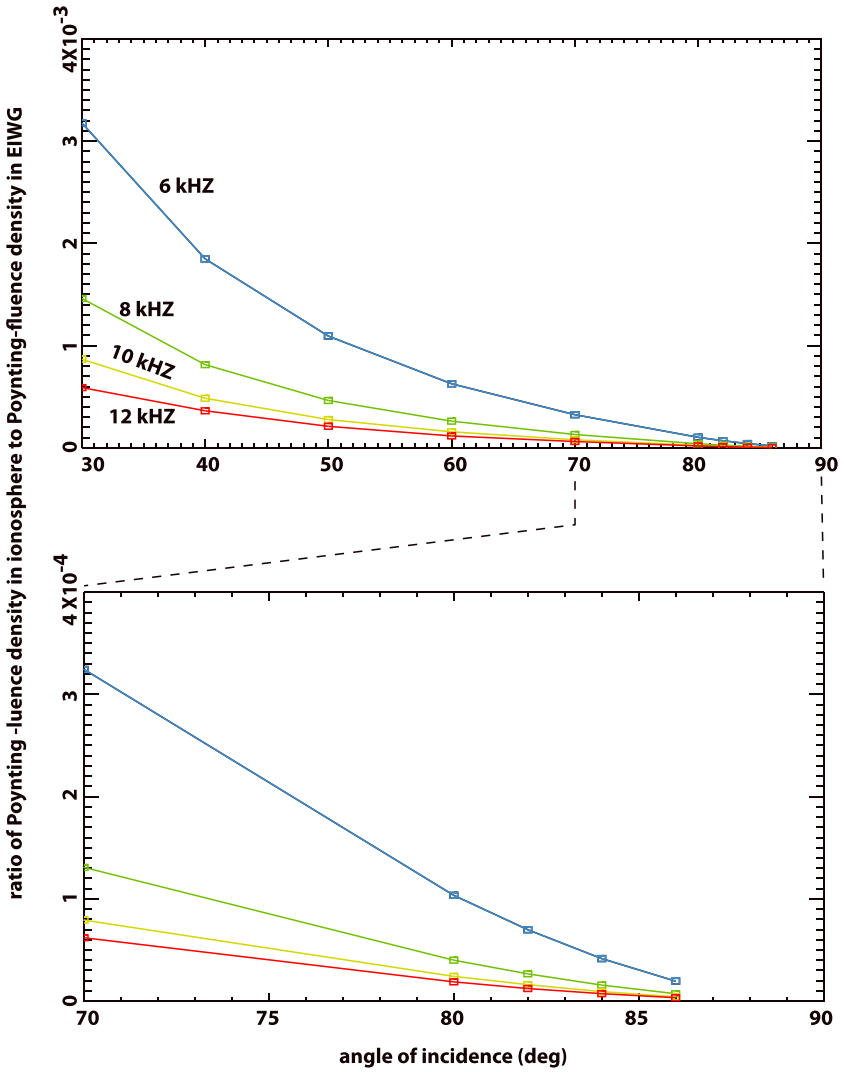

Figure A1. Calculated plane wave energy transmission for midnight *D* layer versus angle of incidence, averaged over propagation magnetic azimuth, for dip angle (magnetic inclination) = 15°. Different curves are for different frequencies in the VEFI passband. The lower panel is a zoom on the range 70° to 90° angle of incidence.

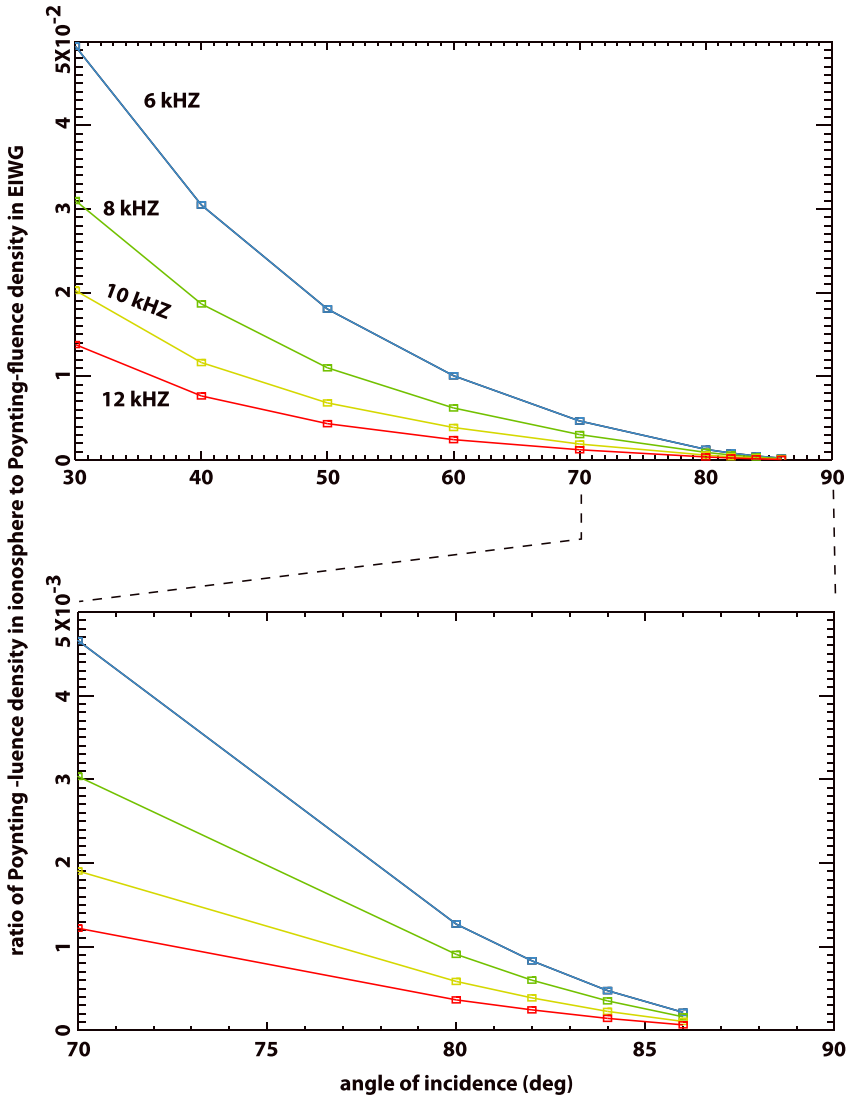

Figure A2. Calculated plane wave energy transmission for midnight *D* layer versus angle of incidence, averaged over propagation magnetic azimuth, for dip angle (magnetic inclination) = 30°. Different curves are for different frequencies in the VEFI passband. The lower panel is a zoom on the range 70° to 90° angle of incidence.

The broadband VLF signals recorded by VEFI have significant spectral content peaking in the region 6–14 kHz (Jacobson et al., 2014, 2016). The frequency centroid is typically around 10 kHz. We run the calculation for typical nighttime conditions (reference height = 87 km and logarithmic derivative of electron density = 0.45 km^{-1} (Jacobson et al., 2009). We run the calculation at all representative azimuths of arrival, in 32 steps of 11.25°. We then average the transmission ratio over all azimuths so as to get an average estimate of the transmission for our azimuth-diverse data.

Figure A1 shows the modeled transmission ratio, averaged over azimuth, for dip angle (magnetic inclination) = 15°. The horizontal axis is angle of incidence, for the domain 30–90° (upper panel) and zoomed (lower panel) to 70–90°. From 30 to 80°, the calculation is done at 10° steps in angle of incidence. From 80 to 86°, the step is 2°. The different-colored curves are for different frequencies, as indicated. Figure A2 is similar but for dip angle = 30°. In the next section we estimate the effective angle of incidence in order to estimate the pertinent modeled transmission ratio from the curves in Figures A1 and A2.

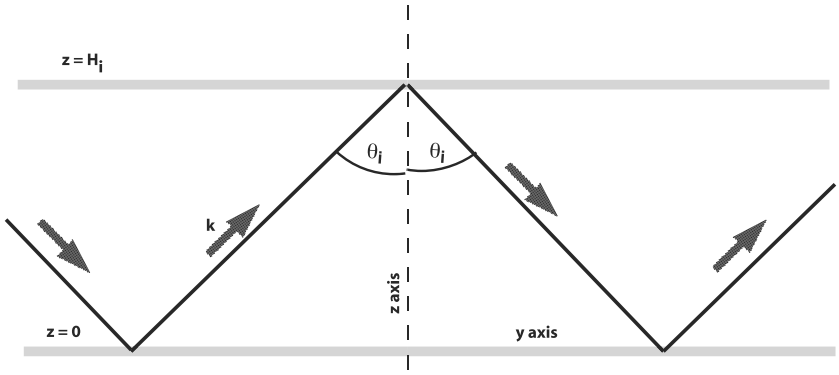

Figure A3. Cartoon of multihop analog of waveguide modes in the Earth-ionosphere waveguide, simplified to a flat-Earth geometry. See text for details.

A.2 Heuristic Estimate of Angles of Incidence and Energy Coupling

The waveguide modes in the EIWG control the VLF propagation from the source (a lightning stroke near ground) to the subsatellite point. The LWPC code calculates these modes in the presence of several complications: variable Earth conductivity, variable ionospheric conductivity, ionospheric geomagnetic anisotropy, and Earth curvature.

The waveguide solutions specify wavefields that can be thought of as a superposition of plane waves. However, the LWPC approach never outputs these plane waves, and nor are they required for any of the code's propagation products. The LWPC outputs information on the propagation along the great circle path but is not concerned with the details of locally oblique wavefields at the underside of the ionosphere. In particular, the LWPC code does not output the wavevector angle, or equivalently the effective "angle of incidence," between the upgoing effective wavevector and the ionospheric normal.

In our present work, however, we seek a rough estimate of the effective "angle of incidence," so that we can exploit the model results in Figures A1 and A2 above, in which the energy transmission is a function of a plane wave's angle of incidence. We will roughly estimate the effective angle of incidence below using a heuristic planar-waveguide model as guidance.

It has been pointed out elsewhere (Cummer, 2000; Dowden et al., 2002) that the basic dispersive behavior of the waveguide solutions may be approximated by an idealized, lossless parallel-plate waveguide model. This is shown in Figure A3, with H_i as the separation between the two conducting planes. This simple waveguide allows both transverse-electric and -magnetic modes. The transverse-magnetic modes are those appropriate to our example, involving waveguide excitation by a short vertical current near the bottom boundary. Each mode's (n = 1, 2, 3, …) dispersion is controlled by its cutoff angular frequency ω_{0n}:

$$k_{hn}^2 = \left(\omega^2 - \omega_{0n}^2\right)/c^2 \tag{A1}$$

Here k_{hn} is the horizontal wavenumber of the nth mode, ω is the wave angular frequency, and ω_{0n} is the mode-cutoff angular frequency given by

$$\omega_{cn} = n\pi c/H_i \tag{A2}$$

Table A2
Effective "Angle of Incidence" (at f = 10 kHz), and Ratio of Ionosphere/EIWG Poynting-Fluence Density, Averaged Over Magnetic Azimuth of Arrival, for First Two Waveguide Modes

	Mode n = 1, θ_i = 80°	Mode n = 2, θ_i = 70°
dip = 30°	ratio = 0.38×10^{-3}	ratio = 1.9×10^{-3}
dip = 15°	ratio = 0.3×10^{-4}	ratio = 0.8×10^{-4}

The free-space wavenumber is $k_{fs} = \omega/c$, so the horizontal wavenumber of the waveguide mode scaled by the free-space wavenumber is

$$\frac{k_{hn}}{k_{fs}} = \sqrt{1 - \frac{\omega_{0n}^2}{\omega^2}} \tag{A3}$$

However, from Figure A3, we see that the horizontal wavenumber of the analogous ray, scaled by the free-space wavenumber, is also equal to the sine of the angle of incidence, from whence equation (A3) implies that the *effective angle of incidence* is

$$\theta_i = \sin^{-1}\left(\sqrt{1 - \frac{\omega_{0n}^2}{\omega^2}}\right) \tag{A4}$$

For the *n*th-mode EIWG solution during night conditions (Dowden et al., 2002), the cutoff frequency is f_{0n} = 1.67n (kHz). Table A2 lists the modeled transmission ratio (at f = 10 kHz) of ionosphere/EIWG Poynting-fluence density, averaged over magnetic azimuth of arrival. The top row of Table A2 lists the effective angle of incidence from equation (A4) for modes n = 1, 2. The middle row lists the transmission ratio for dip = 30°, and the bottom row for dip = 15°. The ratios are obtained by interpolation from Figure A1 (for dip = 15°) and from Figure A2 (for dip = 30°). It is seen that the interpolated ratios are on the order of 10^{-4} for dip = 15°, and 10^{-3} for dip = 30°.

Acknowledgments
This work was partially supported by NSF grant 1443011, "Wave-vector-resolved Study of Lightning Whistler Propagation and Energetics in the Low-latitude Plasmasphere". We are indebted to Michael Hutchins and to Carl Christianson for their work on LWPC waveguide calculations. The authors wish to thank the World Wide Lightning Location Network (http://wwlln.net), a collaboration amongst over 50 universities and institutions, for providing the lightning location data used in this paper. NASA supports public access to CNOFS data via the Web data-portal cdaweb.sci.gsfc.nasa.gov, which is being completed during 2018.

References

Bell, T. F., & Ngo, H. D. (1988). Electrostatic waves stimulated by coherent VLF signals propagating in and near the inner radiation belt. *Journal of Geophysical Research*, *93*(A4), 2599–2618. https://doi.org/10.1029/JA093iA04p02599

Bell, T. F., & Ngo, H. D. (1990). Electrostatic lower hybrid waves excited by electromagnetic whistler mode waves scattering from planar magnetic-field-aligned plasma density irregularities. *Journal of Geophysical Research*, *95*(A1), 149–172. https://doi.org/10.1029/JA095iA01p00149

Bell, T. F., Inan, U. S., Piddyachiy, D., Kulkarni, P., & Parrot, M. (2008). Effects of plasma density irregularities on the pitch angle scattering of radiation belt electrons by signals from ground based VLF transmitters. *Geophysical Research Letters*, *35*, L19103. https://doi.org/10.1029/2008GL034834

Burkholder, B. S., Hutchins, M. L., McCarthy, M. P., & Holzworth, R. H. (2013). Attenuation of lightning-produced sferics in the Earth-ionosphere waveguide and low-altitude ionosphere. *Journal of Geophysical Research: Space Physics*, *118*, 3692–3699. https://doi.org/10.1002/jgra.50351

Christian, H. J., Blakeslee, R. J., Boccippio, D. J., Boeck, W. L., Buechler, D. E., Driscoll, K. T., et al. (2003). Global frequency and distribution of lightning as observed from space by the Optical Transient Detector. *Journal of Geophysical Research*, *108*(D1), 4005. https://doi.org/10.1029/2002JD002347

Cummer, S. A. (2000). Modeling electromagnetic propagation in the Earth-ionosphere waveguide. *IEEE Transactions on Antennas and Propagation*, *48*(9), 1420–1429. https://doi.org/10.1109/8.898776

de La Beaujardiere, O. (2004). C/NOFS: A mission to forecast scintillations. *Journal of Atmospheric and Solar - Terrestrial Physics*, *66*(17), 1573–1591. https://doi.org/10.1016/j.jastp.2004.07.030

Dowden, R. L., Brundell, J. B., & Rodger, C. J. (2002). VLF lightning location by time of group arrival (TOGA) at multiple sites. *Journal of Atmospheric and Solar - Terrestrial Physics*, *64*(7), 817–830. https://doi.org/10.1016/S1364-6826(02)00085-8

Farley, D. T. Jr. (1959). A theory of electrostatic fields in a horizontally stratified ionosphere subject to a vertical magnetic field. *Journal of Geophysical Research*, *64*(9), 1225–1233. https://doi.org/10.1029/JZ064i009p01225

Foust, F. R., Inan, U. S., Bell, T., & Lehtinen, N. G. (2010). Quasi-electrostatic whistler mode wave excitation by linear scattering of EM whistler mode waves from magnetic field-aligned density irregularities. *Journal of Geophysical Research*, *115*, A11310. https://doi.org/10.1029/2010JA015850

Friedrich, M., & Rapp, M. (2009). News from the lower ionosphere: A review of recent developments. *Surveys in Geophysics*, *30*(6), 525–559. https://doi.org/10.1007/s10712-009-9074-2

Heelis, R. A., Coley, W. R., Burrell, A. G., Hairston, M. R., Earle, G. D., Perdue, M. D., et al. (2009). Behavior of the O^+/H^+ transition height during the extreme solar minimum of 2008. *Geophysical Research Letters*, *36*, L00C03. https://doi.org/10.1029/2009GL038652

Helliwell, R. A. (2006). *Whistlers and related ionospheric phenomena* (p. 349). Mineola, New York: Dover Publications.

Hutchins, M. L., Holtzworth, R. H., Rodger, C. J., & Brundell, J. B. (2012). Far-field power of lightning strokes as measured by the World Wide Lightning Location Network. *Journal of Atmospheric and Oceanic Technology*, *29*, 1102–1110. https://doi.org/10.1175/JTECH-D-11-00174

Hutchins, M. L., Jacobson, A. R., Holzworth, R. H., & Brundell, J. B. (2013). Azimuthal dependence of VLF propagation. *Journal of Geophysical Research: Space Physics*, *118*, 1–5. https://doi.org/10.1002/jgra.50533

IAGA, Division V, Working Group 8 (2003). The 9th Generation International Geomagnetic Reference Field. *Earth, Planets and Space*, *55*(8), i–ii.

Jacobson, A. R., Holzworth, R., Harlin, J., Dowden, R., & Lay, E. (2006). Performance assessment of the World Wide Lightning Location Network (WWLLN), using the Los Alamos Sferic Array (LASA) array as ground-truth. *Journal of Atmospheric and Oceanic Technology*, *23*(8), 1082–1092. https://doi.org/10.1175/JTECH1902.1

Jacobson, A. R., Shao, X., & Holzworth, R. H. (2009). Full-wave reflection of lightning long-wave radio pulses from the ionospheric D-region: Numerical model. *Journal of Geophysical Research*, *114*, A03303. https://doi.org/10.1029/2008JA013642

Jacobson, A. R., Holzworth, R., & Shao, X.-M. (2010). Full-wave reflection of lightning long-wave radio pulses from the ionospheric *D*-region: Comparison with midday observations of broadband lightning signals. *Journal of Geophysical Research*, *115*, A00E27. https://doi.org/10.1029/2009JA014540

Jacobson, A. R., Holzworth, R. H., Pfaff, R. F., & McCarthy, M. P. (2011). Study of oblique whistlers in the low-latitude ionosphere, jointly with the C/NOFS satellite and the World-Wide Lightning Location Network. *Annales Geophysicae*, *29*(5), 851–863. https://doi.org/10.5194/angeo-29-851-2011

Jacobson, A. R., Shao, X.-M., & Lay, E. (2012). Time-domain waveform, and azimuth variation, of ionospherically reflected VLF/LF radio emissions from lightning. *Radio Science*, *47*, RS4001. https://doi.org/10.1029/2012RS004980

Jacobson, A. R., Holzworth, R. H., Pfaff, R. F., Heelis, R., & Colestock, P. (2014). A method to estimate whistler wavevector from polarization using 3-component satellite E-field data. *Radio Science*, *49*, 131–145. https://doi.org/10.1002/2013RS005335

Jacobson, A. R., Holzworth, R. H., Pfaff, R., & Heelis, R. (2016). Automated identification of discrete, lightning-generated, multiple-dispersed whistler waves in C/NOFS-VEFI very low frequency observations. *Radio Science*, *51*, 1547–1569. https://doi.org/10.1002/2016RS005989

Lay, E. H., & Shao, X.-M. (2011). High temporal and spatial-resolution detection of D-layer fluctuations by using time-domain lightning waveforms. *Journal of Geophysical Research*, *116*, A01317. https://doi.org/10.1029/2010JA016018

Lay, E. H., Holzworth, R. H., Rodger, C. J., Thomas, J. N., Pinto, O., & Dowden, R. L. (2004). WWLLN global lightning detection system: Regional validation study in Brazil. *Geophysical Research Letters*, *31*, L03102. https://doi.org/10.1029/2003GL018882

Lay, E. H., Jacobson, A. R., Holzworth, R. H., Rodger, C. J., & Dowden, R. L. (2007). Local time variation in land/ocean lightning flash density as measured by the World Wide Lightning Location Network. *Journal of Geophysical Research*, *112*, D13111. https://doi.org/10.1029/2006JD007944

Lay, E. H., Shao, X.-M., & Jacobson, A. R. (2014). D-region electron profiles observed with substantial spatial and temporal change near thunderstorms. *Journal of Geophysical Research: Space Physics*, *119*, 4916–4928. https://doi.org/10.1002/2013JA019430

Lehtinen, N. G., & Inan, U. S. (2009). Full-wave modeling of transionospheric propagation of VLF waves. *Geophysical Research Letters*, *36*, L03104. https://doi.org/10.1029/2008GL036535

Liu, N., Kosar, B., Sadighi, S., Dwyer, J. R., & Rassoul, H. K. (2012). Formation of streamer discharges from an isolated ionization column at subbreakdown conditions. *Physical Review Letters*, *109*(2), 025002-1–025002-5. https://doi.org/10.1103/PhysRevLett.109.025002

Meredith, N. P., Horne, R. B., Clilverd, M. A., Horsfall, D., Thorne, R. M., & Anderson, R. R. (2006). Origins of plasmaspheric hiss. *Journal of Geophysical Research*, *111*, A09217. https://doi.org/10.1029/2006JA011707

Nagano, I., Mambo, M., & Hutatsuishi, G. (1975). Numerical calculation of electromagnetic waves in an anisotropic multilayered medium. *Radio Science*, *10*(6), 611–617. https://doi.org/10.1029/RS010i006p00611

Pappert, R. A., & Ferguson, J. A. (1986). VLF/LF mode conversion model calculations for air to air transmissions in the Earth-ionosphere waveguide. *Radio Science*, *21*(4), 551–558. https://doi.org/10.1029/RS021i004p00551

Pappert, R. A., & Hitney, L. R. (1988). Empirical modeling of nighttime easterly and westerly VLF propagation in the Earth -ionosphere waveguide. *Radio Science*, *23*(4), 599–611. https://doi.org/10.1029/RS023i004p00599

Pfaff, R., Rowland, D., Freudenreich, H., Bromund, K., le, G., Acuña, M., et al. (2010). Observations of DC electric fields in the low-latitude ionosphere and their variations with local time, longitude, and plasma density during extreme solar minimum. *Journal of Geophysical Research*, *115*, A12324. https://doi.org/10.1029/2010JA016023

Piggott, W. R., Pitteway, M. L. V., & Thrane, E. V. (1965). The numerical calculation of wave-fields, reflexion coefficients and polarizations for long radio waves in the lower ionosphere. II. *Philosophical Transactions. Royal Society of London*, *257*(1079), 243–271. https://doi.org/10.1098/rsta.1965.0005

Pitteway, M. L. V. (1965). The numerical calculation of wave-fields, reflexion coefficients and polarizations for long radio waves in the lower ionosphere. I, *Philosophical Transactions. Royal Society of London*, *257*(1079), 219–241.

Rodger, C. J., Brundell, J. B., Dowden, R. L., & Thomson, N. R. (2004). Location accuracy of long distance VLF lightning location network. *Annales de Geophysique*, *22*(3), 747–758. https://doi.org/10.5194/angeo-22-747-2004

Rodger, C. J., Brundell, J. B., & Dowden, R. L. (2005). Location accuracy of VLF World Wide Lightning Location (WWLL) network: Post-algorithm upgrade. *Annales de Geophysique*, *23*(2), 277–290. https://doi.org/10.5194/angeo-23-277-2005

Rodger, C. J., Werner, S., Brundell, J., Lay, E. H., Thomson, N. R., Holzworth, R. H., & Dowden, R. L. (2006). Detection efficiency of the VLF World-Wide Lightning Location Network (WWLLN): Initial case study. *Annales de Geophysique*, *24*(12), 3197–3214. https://doi.org/10.5194/angeo-24-3197-2006

Sonwalkar, V. S., & Inan, U. S. (1989). Lightning as an embryonic source of VLF hiss. *Journal of Geophysical Research*, *94*(A6), 6986–6994. https://doi.org/10.1029/JA094iA06p06986

Starks, M. J., Quinn, R. A., Ginet, G. P., Albert, J. M., Sales, G. S., Reinisch, B. W., & Song, P. (2008). Illumination of the plasmasphere by terrestrial very low frequency transmitters: Model validation. *Journal of Geophysical Research*, *113*, A09320. https://doi.org/10.1029/2008JA013112

Streltsov, A. V., Lampe, M., Manheimer, W., Ganguli, G., & Joyce, G. (2006). Whistler propagation in inhomogeneous plasma. *Journal of Geophysical Research*, *111*, A03216. https://doi.org/10.1029/2005JA011357

Wait, J. R., & Spies, K. P. (1964). NBS technical note 300: Characteristics of the Earth -ionosphere waveguide for VLF radio waves, edited by U. S. D. o. C. National Bureau of Standards (now National Institute of Standards and Technology, NBS.